Supplementary information for

Buried interface molecular hybrid for inverted perovskite solar cells

Sanwan Liu[1,2]†, Jingbai Li[3]†, Wenshan Xiao[4]†, Rui Chen[1]†, Zhenxing Sun[1]†, Yong Zhang[5]†, Xia Lei[5,3], Shuaifeng Hu[6], Manuel Kober-Czerny[6], Jianan Wang[1], Fumeng Ren[1], Qisen Zhou[1], Hasan Raza[1], You Gao[1], Yitong Ji[4], Sibo Li[7], Huan Li[7], Longbin Qiu[7], Wenchao Huang[4,8], Yan Zhao[9,10], Baomin Xu[5], Zonghao Liu[1,2]*, Henry J. Snaith[6], Nam-Gyu Park[11,12]*, Wei Chen[1,2]*

[1]Wuhan National Laboratory for Optoelectronics (WNLO), Huazhong University of Science and Technology (HUST), Wuhan 430074, China.

[2]Optics Valley Laboratory, Hubei, 430074 China.

[3]Hoffmann Institute of Advanced Materials, Shenzhen Polytechnic University, Shenzhen, 518055, China.

[4]Key State Laboratory of Advanced Technology for Materials Synthesis and Processing, School of Materials Science and Engineering, Wuhan University of Technology, 430070, Wuhan, China.

[5]Department of Materials Science and Engineering, Southern University of Science and Technology, Shenzhen, 518055 China.

[6]Clarendon Laboratory, Department of Physics, University of Oxford, Oxford OX13PU, U.K.

[7]Shenzhen Key Laboratory of Intelligent Robotics and Flexible Manufacturing Systems, Department of Mechanical and Energy Engineering, SUSTech Energy Institute for Carbon Neutrality, Southern University of Science and Technology, Shenzhen, 518055, China

[8]Hubei Longzhong Laboratory, Wuhan University of Technology Xiangyang Demonstration Zone, 441000, Xiangyang, China.

[9]College of Materials Science and Engineering, Sichuan University, Chengdu 610065, China.

[10]The Institute of Technological Sciences, Wuhan University, Hubei, Wuhan 430072, China.

[11]School of Chemical Engineering and Center for Antibonding Regulated Crystals, Sungkyunkwan University (SKKU), Suwon 16419, Republic of Korea.

[12]SKKU Institute of Energy Science & Technology (SIEST), Sungkyunkwan University, Suwon 16419, Republic of Korea.

†These authors contributed equally to this work.

*Corresponding authors. E-mail: liuzonghao@hust.edu.cn; npark@skku.edu; wnlochenwei@hust.edu.cn.

This PDF file includes:

Supplementary Notes 1-12

Supplementary Figs. 1-51

Supplementary Tables 1-12

Supplementary References 1-40

Contents

Supplementary Note 1: Computational details

Heterojunction models

The heterojunction model contains the perovskite, SAM, and NiO layers. The perovskite layer used a 16 × 17 × 3 $FAPbI_3$ slab and the NiO layer used a 25 × 26 × 2 NiO slab, which produced a 104.5 Å × 108.8 Å surface. We set a 20.0 Å layer for the SAM layer to provide sufficient space for simulating their movements between the perovskite and NiO surfaces. Given the 3:1 molar ratio between the Me-4PACz and carboxylic acids in the experiments, we considered four cases for the SAM layers: (i) 90 Me-4PACz molecules, (ii) 90 Me-4PACz and 30 BA molecules, (iii) 90 Me-4PACz and 30 NA molecules, (iv) 90 Me-4PACz and 30 TA molecules. The molecular configurations of Me-4PACz, BA, NA, and TA were randomly generated between the perovskite and NiO layers using the Packmol program[1]. The heterojunction models consisted of 24242, 24692, 25532, and 24872 atoms for the Me-4PACz only, BA-Me, NA-Me, and TA-Me hybrid systems, respectively. The top two atom layers of the perovskite and the bottom two atom layers of the NiO surface were fixed to approximate the bulk parts of the perovskite and NiO film. It helps maintain the distance between the films. The periodic boundary conditions were applied to the x and y directions.

Molecular dynamics simulations

We performed classical molecular dynamics simulations for the perovskite/SAMs/NiO heterojunction using the LAMMPS program[2]. The equation of motions was integrated with a time step of 1 fs using the Velocity Verlet method[3]. The trajectories were simulated in a canonical ensemble (NVT) with the Nosé-Hoover thermostat[4,5], with a time constant of 0.1 fs. We first minimized the heterojunction structures using the conjugated gradient method. Then, we prepared the initial conditions for the molecular configurations and velocities of all unfixed atoms in the heterojunction models by simulating the annealing process in the device fabrication. The velocities were initialized at 400 K and equilibrated in 10 ps, cooled to 298.15 K in the subsequent 10 ps, and then further equilibrated at 298.15 K in another 10 ps. In the production run, the initial conditions were equilibrated in 0.5 ns at 298.15 K. The last snapshots were used to sample the molecular clusters, and adsorption structures and analyze the surface coverage ratio using our in-house code. We assigned the SAMs to the adjacent surface according to the distance between their geometrical

center and the surface, based on a threshold of 10 Å. The surface coverage calculations identified the surface area covered by the atoms of the SAMs less than 5 Å to the surface, with a 2 Å radial threshold.

The interactions of the perovskite surface employed the recently developed transferable perovskite force field[6]. The interactions of SAMs used the DREIDING force fields[7]. The atomic charges for the DREIDING force fields used the restrained electrostatic potential (RESP) charges[8], computed at the PBE0/cc-pVDZ level, using the ORCA 5.0.3 program[9]. The interactions between the perovskite and SAMs use the universal force field[10]. The NiO surface was described by the INTERFACE force field[11], which showed good compatibility with the DREIDING force field for simulating molecular adsorptions on metal oxides. Detailed distance cutoffs for the electrostatic and non-bonding interactions are available in the literature cited above. The interactions between the perovskite and NiO surfaces were ignored as their interactions are negligible at a distance of about 20 Å.

The molecular dynamics simulations for the heterojunctions with perovskite surface defects used the same setting as the adsorption simulation, except that we created a charged Pb vacancy on the perovskite surface. The position of the surrounding I atoms was also fixed to maintain the Pb vacancy, which allow us to monitor the interactions between the SAMs and the charged defects for sampling the molecular configurations of SAMs at the passivated defects.

DFT calculations

The geometry optimizations for bulk, slabs, surface adsorptions, molecular clusters, intrinsic surface defects, and passivated surface defects used the VASP code[12] with a plane wave (PW) basis set and projected augmented wave (PAW) pseudopotentials (PPs). We employed the PBE flavor of the GGA PPs, and long-range dispersion interactions were considered by the DFTD3 scheme. The kinetic energy cut-off is 500 eV for the expansion of the wavefunctions. The convergence thresholds were set to 10^{-6} eV for energy and 0.05 eV $Å^{-1}$ for the norm of the atomic forces.

The cell parameters for cubic NiO and α-phase (orthorhombic) perovskite were optimized with a 6 × 6 × 6 and 4 × 4 × 4 k-point mesh centered at the Gamma point, respectively. The optimized parameters are a = b = c = 4.14310 Å, and α = β = γ = 90° for NiO and a = 6.45684 Å, b = 6.32134 Å, c = 6.39278 Å, and α = β = γ = 90° for $FAPbI_3$. We performed the adsorption calculations on the

(100) surface of the perovskite and NiO, based on a 3 × 3 × 2 $FAPbI_3$ slab and a 5 × 5 × 2 NiO slab, respectively. The ionic optimizations fixed the bottom two atom layers to represent the bulk structures. We added a 17 Å and 14 Å vacuum space to the perovskite and NiO slabs to avoid artificial interactions between the neighboring cells. Dipole corrections are applied to the z-direction to eliminate the artificial electrostatic interactions between the asymmetric repeated slabs. The Hubbard corrections, U = 8 eV and J = 0.95 eV were used for Ni to account for the strong electron correlations in 3d orbitals[13]. All adsorption calculations were done at the gamma point. The adsorption energy (ΔE_{ads}) is defined as

$$\Delta E_{ads} = E_{\text{slab+molecule}} - E_{slab} - E_{molecule}$$

Where E_{slab} and $E_{molecule}$ are the dipole-corrected electronic energy of the slab and adsorbed molecule, respectively. The binding energy ($\Delta E_{binding}$) for molecular clusters is defined as

$$\Delta E_{binding} = \frac{E_{\text{cluster}} - N \cdot E_{monomer}}{N}$$

where $E_{monomer}$ is the electronic energy of the single molecule. N is the number of molecules in the cluster.

The perovskite surface defect calculations used the 3 × 3 × 2 $FAPbI_3$ slab. We created the I-vacancy (V_I), Pb-vacancy (V_{Pb}), Pb–I antisite (Pb_I), and I–Pb antisite (I_{Pb}) on the surface with various numbers of point charges. The ions were optimized using the gamma point and the charge density was recomputed with a 2 × 2 × 1 k-point mesh centered at the gamma point for band structure calculations. The electronic energies and the valence band maxima were used to compute the defect formation energies and defect transition levels. The defect formation energy ($\Delta E_{formation}$) of the perovskite slab is define as

$$\Delta E_{formation} = E_{\text{defect}} - E_{slab} - \sum_i n_i \mu_i + q(\varepsilon_F + \varepsilon_{VBM} + \Delta v)$$

where E_{defect} and E_{slab} are the electronic energies for the defective and perfect slab. For each species, i, n_i, and μ_I are the numbers of added atoms (n_i>0) and the chemical potential. n_i<0 for removed atoms. q is the defect charge state. ε_F is the Fermi energy referenced to the valence band maximum of the slab. ε_{VBM} is the energy of the valence band maximum. Δv aligns the electrostatic potential of the perfect and defective slab. The defect transition levels are computed by solving the ε_F leading to identical defection formation energies of two charge states.

$$\Delta E_{formation}(q_0) = \Delta E_{formation}(q_1)$$

$$\varepsilon_F(q_0/q_1) = \frac{E_{\text{defect}}(q_0) - E_{\text{defect}}(q_1)}{q_1 - q_0} - (\varepsilon_{\text{VBM}} + \Delta v)$$

The calculations for the passivated V_{Pb}^{2+} surface defect used the same settings as the surface defect calculations. We computed the binding energies of molecules to the V_{Pb}^{2+} on the perovskite surface using the same equation as the adsorption energy without dipole corrections because the dipole moment of a charged surface is no longer gauge-independent. Thus, the binding energies were only used to qualitatively compare the interactions between SAMs and the V_{Pb}^{2+} defect.

Supplementary Note 2: Analysis of Supplementary Fig. 4

The Me-4PACz tetramer shows notable hydrogen bonding networks between the phosphonic groups, which caused the agglomeration of SAMs accompanied with nanovoids. The structures of NA and Me-4PACz were well fitted to form hydrogen bonding with non-bonding interactions, such as the CH (the H atom of the benzene ring of NA molecule)…π, π-π interactions. The formation of NA-Me dimer reduces the formation of the Me-4PACz clusters, providing a compact HSL to grow the perovskite crystal with high surface coverage. A high surface coverage is also good for surface defect passivation.

Supplementary Note 3: Residual stress analysis by GIXRD

For GIXRD measurement, the (210) plane of perovskite featuring an XRD peak at 31.6° was selected was chosen as the stress-free 2θ degree due to its diversity in providing more reliable structure symmetry information, in which the 2θ is fixed while the instrument tilt angles were varied to ensure the X-ray penetration depth. The tilt angles (ψ) were fixed at 5°, 15°, 25°, 35°, and 45°, respectively. According to Bragg's Law and generalized Hooke's Law, the relationship of 2θ-$\sin^2\psi$ can be given by the following equation[14]:

$$\sigma = -\frac{E_p}{(1+\nu_p)}\frac{\pi}{180^\circ}\cot\theta_0\frac{\partial(2\theta)}{\partial[(\sin\Psi)^2]} \quad \text{(S1)}$$

where E_p is the perovskite modulus (10 GPa) and ν_p is Poisson's ratio of the perovskite (0.3)[15]. θ_0 is half of the scattering angle $2\theta_0$ for stress-free perovskite ($2\theta_0$ = 31.6°). The residue stress of perovskite films can be calculated from equation (S1) by fitting the 2θ as a function of $\sin^2\psi$, and the slope of the fitted line represents the scale of the residual strain. The negative slope indicates the films bear tensile stress, while the positive slope indicates the films bear compressive stress.

Supplementary Note 4: Analysis of Supplementary Fig. 18

We further investigated the charge transfer and recombination kinetics of perovskite films on studied HSLs by carrying out steady-state photoluminescence (PL) and time-resolved PL (TRPL) measurements. Obviously, the perovskite film on NA-Me shows a higher PL intensity and longer τ_2 (661.3 ns) than those on Me-4PACz (310.1 ns), BA-Me (389.8 ns) and TA-Me (593.6 ns), respectively, where the longer τ_2 is likely related to suppressed interfacial nonradiative recombination, which suggests that there are minimal nonradiative recombination losses at the buried interface where the NA-Me is located. We further use a differential lifetime (τ) to help distinguish the charge transfer and SRH recombination more clearly as the following equation:

$$\tau = -\{d\ln[\varphi(t)]/dt\}^{-1} \quad \text{(S2)}$$

where $\varphi(t)$ is the time-dependent PL photon flux. The differential lifetime was calculated by using fits to the TRPL transients. As shown in Supplementary Fig. 18c, the sharp rise in the τ of the NA-Me at an early stage strongly indicates an efficient charge transfer process. The transition from increasing lifetime to the plateau implies that SRH recombination becomes dominant[16]. Combining these data, we conclude that the NA-Me not only provides a faster charge extraction but also significantly reduces the interfacial trap density.

Supplementary Note 5: Calculation of the quasi-Fermi level splitting (QFLS) based on the PL quantum yield (PLQY)

To investigate the non-radiative recombination at the interface between different hole-selective layers and perovskite, we calculated the Quasi-Fermi level splitting (QFLS) values of 1.53-eV bandgap perovskite films on a bare glass substrate and different HSLs on the ITO substrate by using photoluminescence quantum yield (PLQY) measurements. Dieter Neher et al. summarized a direct relation between QFLS and PLQY as the following equation[17]:

$$\mathrm{QFLS} = \mathrm{QFLS_{rad}} + k_B T \cdot \ln(\mathrm{PLQY}) = k_B T \cdot \ln\left(\mathrm{PLQY}\frac{J_G}{J_{0,rad}}\right) \quad \text{(S3)}$$

Here, QFLS is the difference between the electron and hole quasi-Fermi levels in the perovskite layer, k_B is the Boltzmann constant, and T is the temperature (300 K). J_G is the generation current density under illumination, in this case, approximated to the short-circuit current density J_{SC} of devices. $J_{0,rad}$ is the dark radiative recombination saturation current density.

According to the detailed balance at open-circuit conditions, the $J_{0,rad}$ can be calculated by the following equations:

$$J_{0,rad} = e\int_0^\infty \mathrm{EQE_{PV}}(E)\,\Phi_{BB}(E)dE \quad \text{(S4)}$$

$$\Phi_{BB}(E) = \frac{2\pi E^2}{h^3 c^2}\cdot\frac{1}{exp\left(\frac{E}{k_B T}\right)-1} \quad \text{(S5)}$$

Where e is the elementary charge, EQE_{PV} is the photovoltaic external quantum efficiency, E is the photon energy, ϕ_{BB} is the black-body radiative spectrum, h is the Planck constant, and c is the light speed in a vacuum.

External quantum efficiency (EQE) of the p-i-n PSCs and the emitted spectral photon flux are calculated when the device is in equilibrium with the black-body (BB) radiation (T = 300 K). Based on equations S4 and S5, the $J_{0,rad}$ was calculated similarly as 4.72×10^{-20} A m^{-2} for all systems independent of the bottom charge transport layer. Subsequently, combined with the PLQY value of the samples with the different HSLs underneath, the QFLS of the samples can be obtained according to equation S3. Besides, the V_{OC} non-radiation recombination loss $\Delta V_{OC}^{non-rad}$ can be obtained according to the following equation:

$$\Delta V_{OC}^{non-rad} = \frac{QFLS_{rad} - QFLS}{e} = -\frac{k_B T \ln(PLQY)}{e} \quad \text{(S6)}$$

Supplementary Note 6: Modelling of the light intensity-dependent PLQE (two-trap level SRH model)

In order to further disentangle the effects of surface recombination and bulk recombination via deep and shallow traps, we measured intensity-dependent PLQE of the Me-4PACz and NA-Me samples. The internal PLQE can be described via:

$$PLQE_{\text{int}} = \frac{k_{rad} n_{eq}}{k_{rad} n_{eq} + k_{tr} \cdot \frac{n_{eq}}{2 \cdot n_{eq} + n_{em}} + k_{deep}} \tag{S7}$$

where k_{rad} is the radiative bimolecular recombination rate, k_{deep} is the non-radiative recombination rate via a deep trap level, k_{tr} is the trapping rate into a shallow trap level, and n_{em} is the density of charge carriers emitted from the shallow trap level. Here, k_{deep} can stem from both, a deep surface or bulk trap. n_{em} is related to the energetic depth of the trap (ΔE_{t}) via:

$$n_{em} = N_C \cdot e^{-\Delta E_t / k_B T} \tag{S8))}$$

N_{C} is the density of states in the conduction band and assumed to be 10^{18} cm^{-3} here. In equation S9, n_{eq} is the equilibrium carrier concentration under the continuous illumination used in the PLQE measurement and can be obtained by solving:

$$\frac{dn}{dt} = 0 = G - k_{rad} {n_{eq}}^2 - k_{tr} \cdot \frac{{n_{eq}}^2}{2 \cdot n_{eq} + n_{em}} - k_{deep} \cdot n_{eq} \tag{S9}$$

where G is the generation rate of charge carriers. It is obtained from the laser intensity, spot size and perovskite thickness. In accordance with the previous work[18], external PLQE is then described by:

$$PLQE_{\text{ext}} = \frac{P_{esc} \cdot PLQE_{int}}{(1 - PLQE_{int}) + (P_{esc} \cdot PLQE_{int})} \tag{S10}$$

where P_{esc} is the escape probability of a photon generated within the perovskite material. We solve these equations iteratively for each generation rate to extract the parameters from the data. In total, 5 parameters are described for each sample (10 in total). This is a lot, considering that we could only measure 9 intensities. We thus, reduce the number of free parameters, by sharing some of them between both samples: k_{rad} is a material property and hence should not change between samples, P_{esc} depends more on the substrate, and the energetic depth of the trap ΔE_{t}, which we share between the samples for clarity of the results. The resulting fitted external PLQE is shown in Fig. 3h as a function of absorbed photon flux. We obtained 7 parameters, which are summarized in Supplementary Table 4.

We found that both, the trapping rate k_{tr} and the non-radiative recombination rate k_{deep} decrease for the NA-Me sample. k_{deep} is the total recombination rate via deep traps level as:

$$k_{deep} = k_{bulk,deep} + k_{surface,deep} \tag{S11}$$

In combination with the TRPL shown in Supplementary Fig. 18b, we interpreted this result as an increase in surface recombination, for the Me-4PACz sample, which results in a fast early-time TRPL decay. In addition, k_{tr} is also reduced for the NA-Me sample. It is dependent on the trap density N_t via:

$$k_{tr} = v_T \sigma_t N_t \tag{S12}$$

with v_T the thermal velocity and σ_t the capture cross-section of the trap, both of which are expected to be constant between the samples. The reduced trapping rate is thus interpreted as a reduced density of shallow traps.

Supplementary Note 7: Analysis of Supplementary Fig. 25

Defect formation energy depends on the chemical potential of Pb and I. Thus, it is essential to determine the chemical environment in the experiment. We considered a Pb and I-moderate condition because the UPS results (Supplementary Fig. 16) showed a *p*-type perovskite bottom surface. To better compare the deformation energies of various defects, we plot the defect transition level diagram in Supplementary Fig. 25. At the Pb and I-moderate conditions (Supplementary Table 5), all V_I and V_{Pb} defects show negative formation energies (thermodynamically favored). All Pb_I defects are thermally unstable, suggesting a low formation possibility. The I_{Pb}^{-1} defects show comparable formation energy (–1.35 eV) to the V_I (–(1.09-1.68) eV) and V_{Pb} defects (–(1.00-1.20) eV). The band structures in Supplementary Fig. 24 show all V_I defects lead to shallow trap states, which seem not to introduce significant nonradiative recombination. The V_{Pb}^{2+} defect shows deep trap states, while the others only involve shallow traps. The I_{Pb}^{-1} defect shows a deep trap state in part of the slab. Collectively, the V_{Pb}^{2+} defects generated the most notable trap state, which could be the primary source of nonradiative recombination. Thus, we mainly investigated the passivation mechanism for the V_{Pb}^{2+} defect.

Supplementary Note 8: Analysis of Supplementary Fig. 27

NA remained significantly higher distributions near the perovskite surface than the BA and TA after equilibrating the V_{Pb}^{2+} defective heterojunction models. These results confirmed strong adsorptions of TA and BA on NiO, consistent with the MD simulations without the defects. We found the Me-4PACz coverage on perovskite in the NA-Me hybrid is slightly lower than that in pure Me-4PACz. It suggests the formation of the V_{Pb}^{2+} defect could reduce the adsorbability of Me-4PACz on the perovskite surface when mixed with NA. However, NA-Me still showed the highest overall perovskite surface coverage. These results suggest NA helped maintain the perovskite surface coverage when the adsorbability of Me-4PACz decreased, underscoring the superiority of NA-Me HSL.

Supplementary Note 9: Analysis of Supplementary Fig. 31

When Me-4PACz's π-ring attached to the V_{Pb}^{2+} is defective, the two deep traps become one shallow trap with a lowered deep trap. This finding provided a reasonable explanation for the reduced nonradiative recombination observed in the experiment. The differential charge density for Me-C2 clearly shows charge transfer from Me-4PACz's π-ring to the V_{Pb}^{2+} defect on the perovskite surface. This is because Me-4PACz's π-ring is electron-rich and can extract the positive charges from the defective surface. As a result, it partially restored the I–Pb bond and passivated the V_{Pb}^{2+} deep trap.

Supplementary Note 10: Analysis of Supplementary Fig. 33

It should be noted that thanks to the booming development of SAM, the efficiency and stability of inverted PSCs have been rapidly improved. Me-4PACz is a well-known SAM with excellent function of hole transport and suppressing interfacial nonradiative recombination, which is the foundation of the molecular hybrid structure and plays an important role. The other two aromatic carboxylic acid molecules, BA and TA do not have electron-donating groups, so they can't act as typical HSLs. Although NA has electron-donating groups (triphenylamine functional groups), their carboxyl group (electron-withdrawing group) directly connects to the triphenylamine unit, reducing their potential as an HSL. Therefore, the BA/TA/NA molecule cannot serve as SAM like Me-4PACz, which is further reflected in the significant differences in the performance of their devices (ITO/Me-4PACz (or BA or TA or NA)/perovskite/PI/PCBM/BCP/Ag, Supplementary Fig. 33a). BA, TA, and NA samples only yielded PCEs of 12.17%, 13.08%, and 14.27%, respectively, which are far lower than that of the Me-4PACz sample (22.85%). On the other hand, due to the presence of carboxyl groups, the three aromatic carboxylic acids can anchor on the surface of NiO, which can play a certain role in suppressing defects at the NiO/perovskite interface, thereby improving the efficiency of NiO-based inverted PSCs to a certain extent (ITO/NiO/BA (TA or NA)/perovskite/PI/PCBM/BCP/Ag, Supplementary Fig. 33b). These results further reflect the importance of the molecular hybrid strategy.

Supplementary Note 11: Analysis of Supplementary Table 9

As far as the molecular hybrid is concerned, it has been successful in improving the performance of single-junction inverted PSCs. Although some literature has reported molecular hybrid strategies in inverted PSCs, few works systematically compare the effects of multiple hybrid molecules on SAM, as we have done in our work. For example, Amran Al-Ashouri et al. overcame the wettability of Me-4PACz by adding the 6-hexylenediphosphonic acid (6dPA) to the SAM precursor solution and achieved a PCE of 20.9% with a triple-halide perovskite (bandgap:1.68 eV)[19]. Alex K.-Y. Jen et al. optimized recombination loss at the hole-selective interface in inverted PSCs by developing a co-assembled monolayer (co-SAM, ((2,7-dimethoxy-9H-carba-zol-9-yl)methyl)phosphonic acid (DC-PA)+alkyl ammonium containing 6-(iodo-λ^5-azanyl)hexanoic acid (IAHA))[20]. Correspondingly, this co-SAM approach achieved a decent PCE of 23.59% with a triple-cation perovskite (bandgap: approximately 1.55 eV). In particular, Edward H. Sargent et al. developed a conformal SAM as the hole-selective contact on light-managing textured substrates[21]. They confirmed the important role of molecular hybrid strategy in increasing the coverage of SAM on the FTO surface and suppressing nonradiative recombination at the buried interface. In addition, this molecular hybrid strategy achieved a certified quasi-steady-state PCE of 24.8% for inverted PSCs (bandgap: approximately 1.53 eV). Compared with the aforementioned molecular hybrid strategies, the molecules proposed in our work are carboxylic acid functionalized aromatic molecules, while the aforementioned molecules are all functionalized aliphatic compounds with anchoring groups. The strong π-π interaction and hydrogen bonding between Me-4PACz and the triphenylamine moiety in the NA molecule will reduce the formation of the Me-4PACz clusters, thus improving the coverage of mixed SAMs at the NiO/perovskite interface. We focused on studying the effects of homogeneous SAMs on the morphology and nonradiative recombination of buried interfaces, and we also considered the scale-up ability of optimal mixed SAMs. This strategy delivers a record-certified steady-state efficiency of 26.54% and 23.06% (certified 22.74%) for small-area PSCs and mini-modules with an aperture area of 11.1 cm^2, respectively. Therefore, we have added a more detailed comparison with recent research on SAMs, especially those involving molecular hybrids for inverted PSCs in Supplementary Table 9.

Supplementary Note 12: Fill factor (FF) loss analysis

Following the assumption of the S-Q limit, FF losses are determined by two main components: non-radiative loss and charge transport loss[22]. The higher the maximum FF (FF_{max}) value, the lower the nonradiative recombination loss of the device. The FF_{max} can be empirically calculated according to the following equation:

$$FF_{max} = \frac{v_{OC} - \ln(v_{OC} + 0.72)}{v_{OC} + 1} \quad \text{(S13)}$$

Where $v_{OC} = \frac{V_{OC}}{nK_BT/q}$, K_B is Boltzmann constant, T is temperature (300 K), q is elementary charge. n is the ideality factor that is extracted from the V_{OC} as a function of light intensity on a logarithmic scale, which is shown in Supplementary Fig. 40.

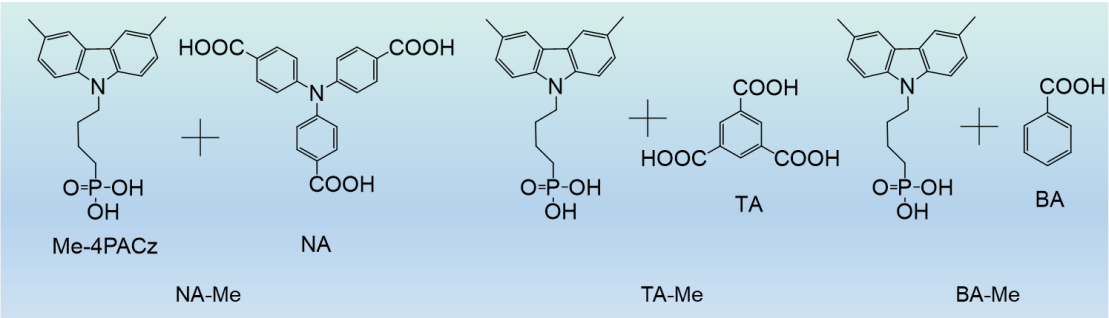

Supplementary Fig. 1. The structure of three mixed SAMs.

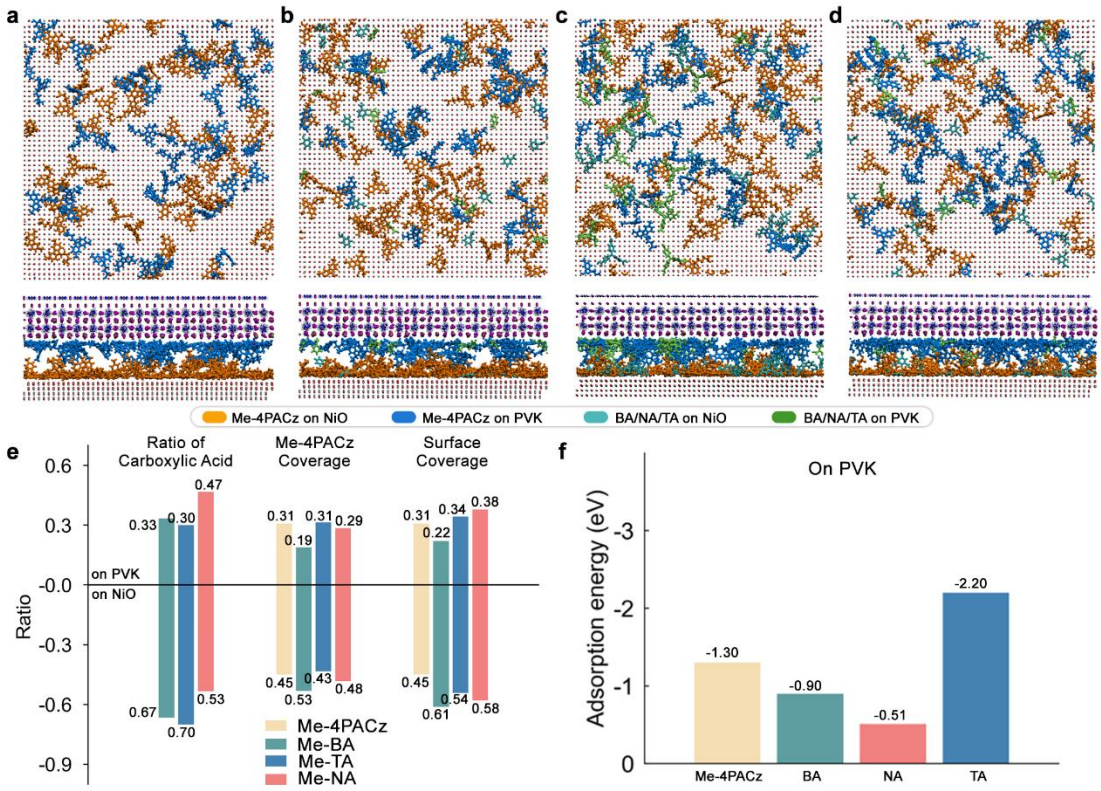

Supplementary Fig. 2. Top and side views of initial molecular representations for the heterojunctions with only Me-4PACz (**a**), BA-Me (**b**), NA-Me (**c**), and TA-Me hybrid (**d**). **e**. Adsorption analysis for the perovskite and NiO surface in the initial conditions of the heterojunction models. **f.** Adsorption energies for SAMs on perovskite surface. The low adsorbability of NA on the perovskite surface could facilitate their interactions with Me-4PACz. Mixing of NA and Me-4PACz will reduce the number of Me-4PACz tetramers, leading to compact HSL with minimized nanovoids.

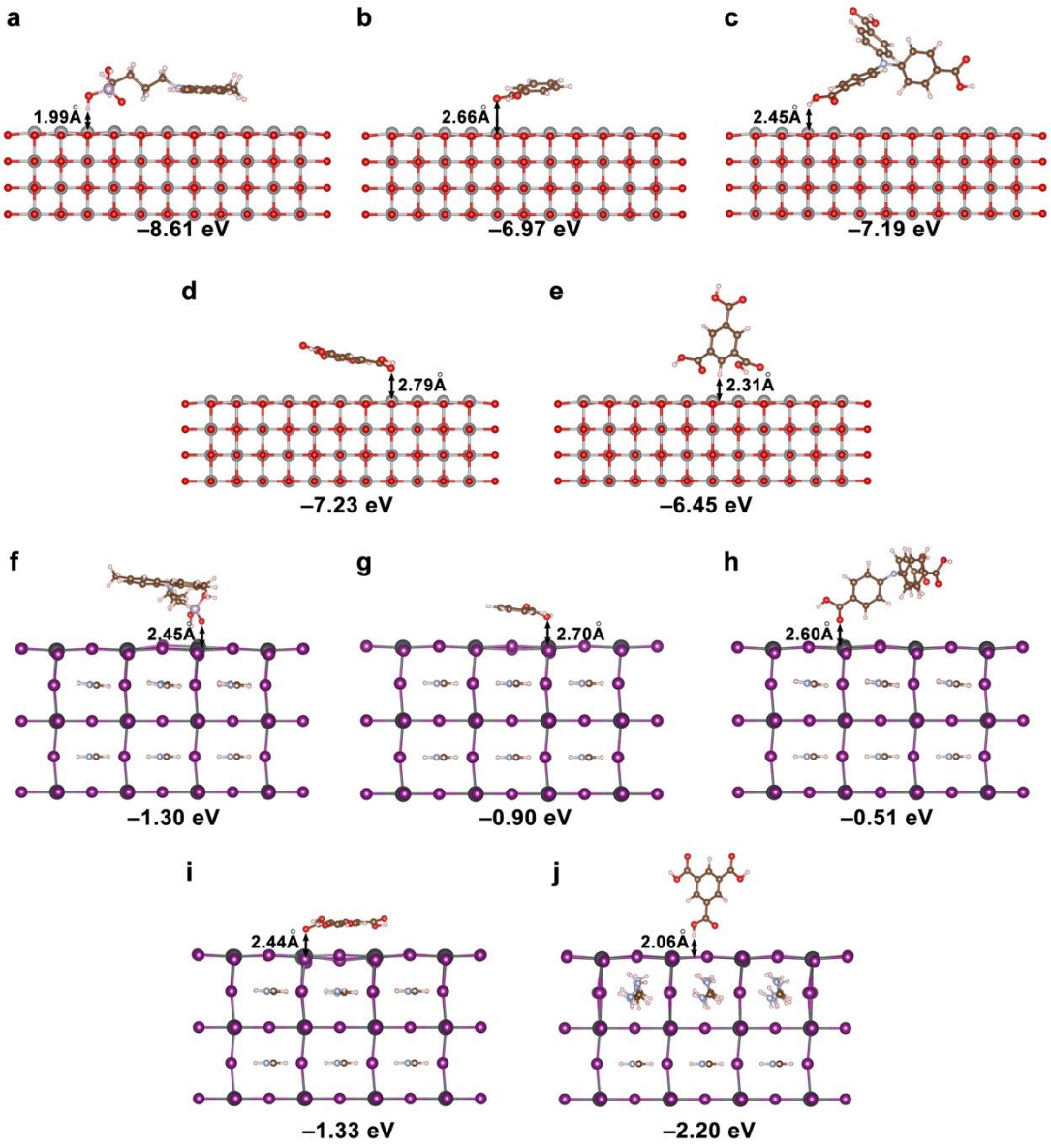

Supplementary Fig. 3. Optimized structures for the adsorption of (**a**) Me-4PACz, (**b**) BA, (**c**) NA, (**d**) parallel TA, and (**e**) vertical TA on the surface of the NiO slab, respectively. Optimized structures for the adsorption of (**f**) Me-4PACz, (**g**) BA, (**h**) NA, (**i**) parallel TA, and (**j**) vertical TA on the surface of the perovskite slab, respectively. The molecular configurations of SAMs were sampled from MD simulations for the heterojunction models. The shortest distance between SAMs and slabs is highlighted in each structure, and the adsorption energies are given below.

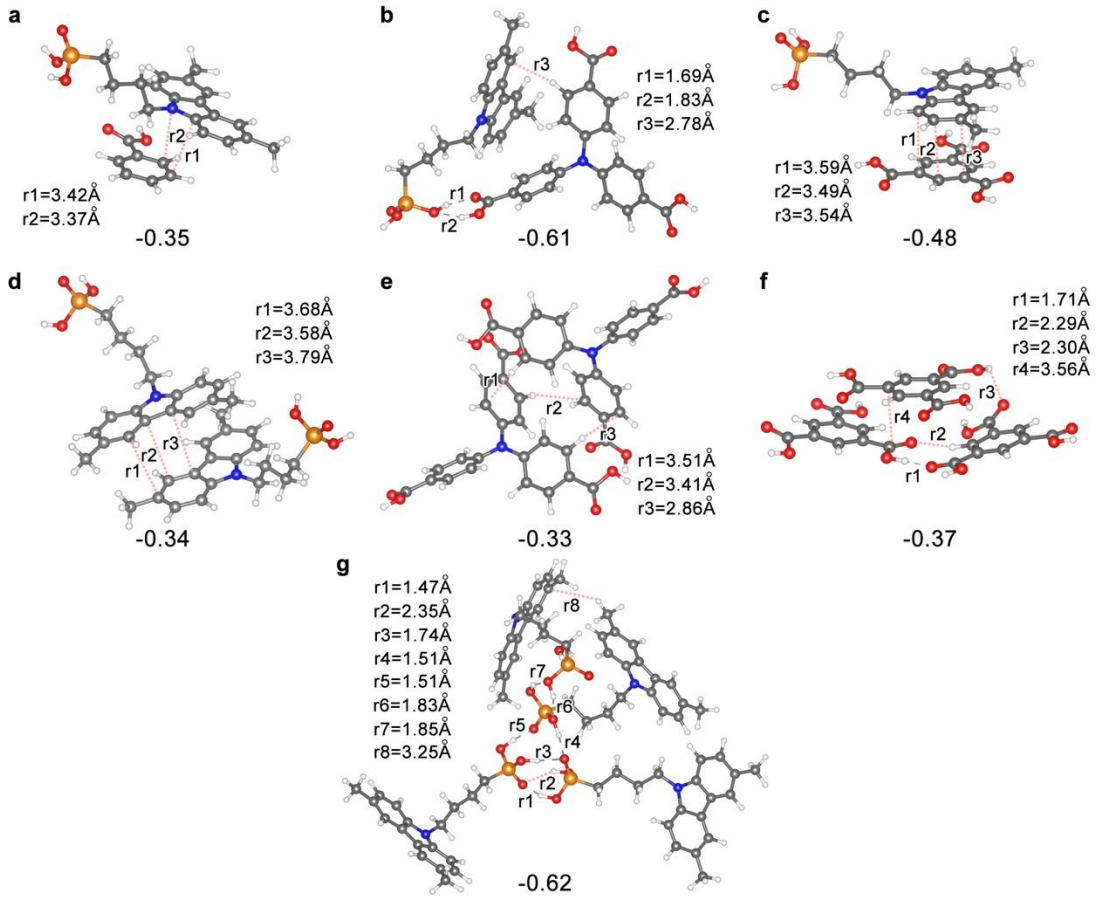

Supplementary Fig. 4. Optimized structures of the (**a**) BA-Me dimer, (**b**) NA-Me dimer, (**c**) TA-Me dimer, (**d**) Me-Me dimer, (**e**) NA-NA dimer, (**f**) TA trimers, and Me-4PACz tetramer observed in MD simulations. Critical intermolecular distances are highlighted aside from the structure and the binding energy is given below.

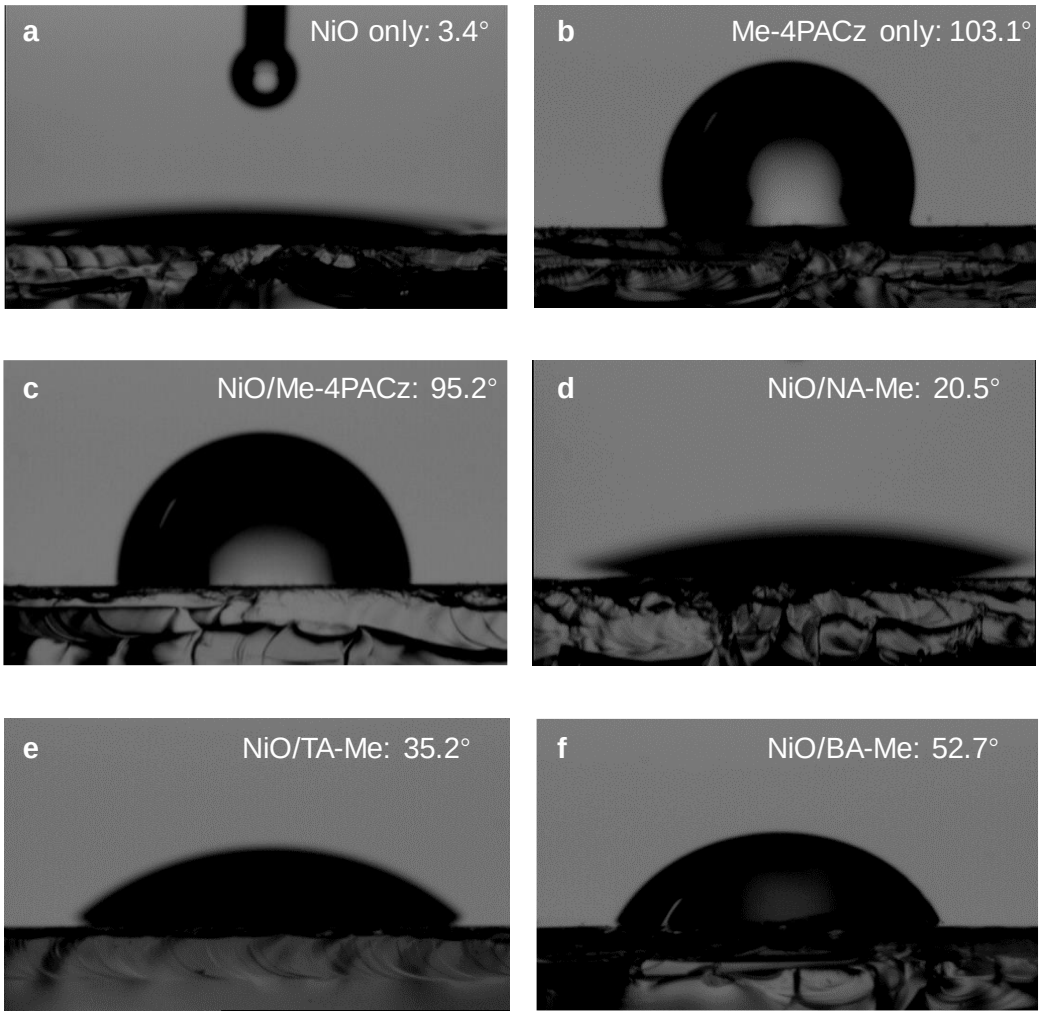

Supplementary Fig. 5. Water contact angle on (**a**) NiO only, (**b**) Me-PACz only, (**c**) NiO/Me-4PACz, (**d**) NiO/NA-Me, (**e**) NiO/TA-Me, and (**f**) NiO/BA-Me.

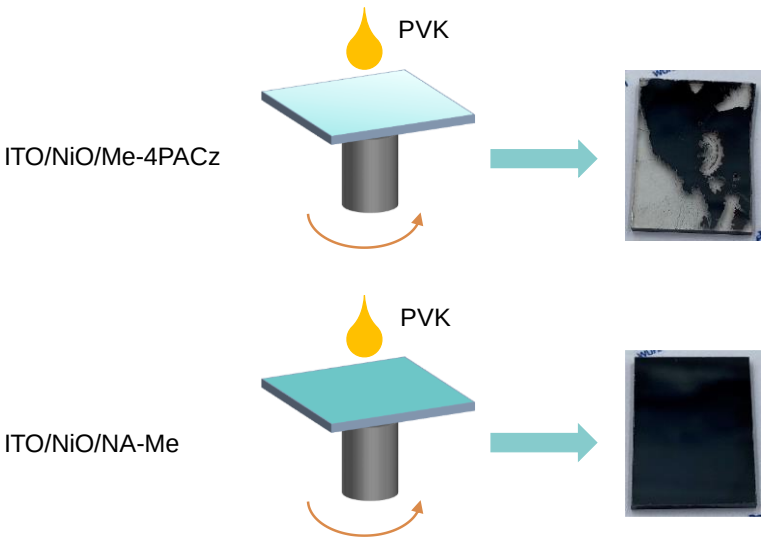

Supplementary Fig. 6. Images of perovskite films coverage on Me-4PACz and NA-Me HSLs.

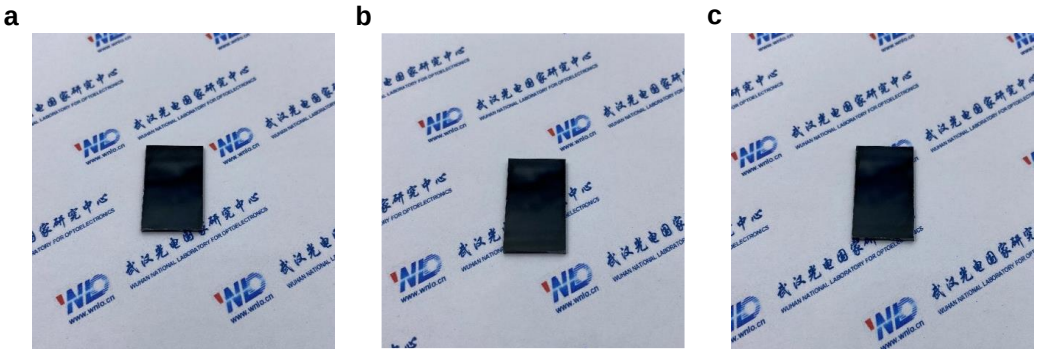

Supplementary Fig. 7. Images of perovskite film coverage on different HSLs. **a**, NiO, **b,** NiO/BA-Me, and **c**, NiO/TA-Me. PVK: $FA_{0.95}Cs_{0.05}PbI_3$ perovskite film.

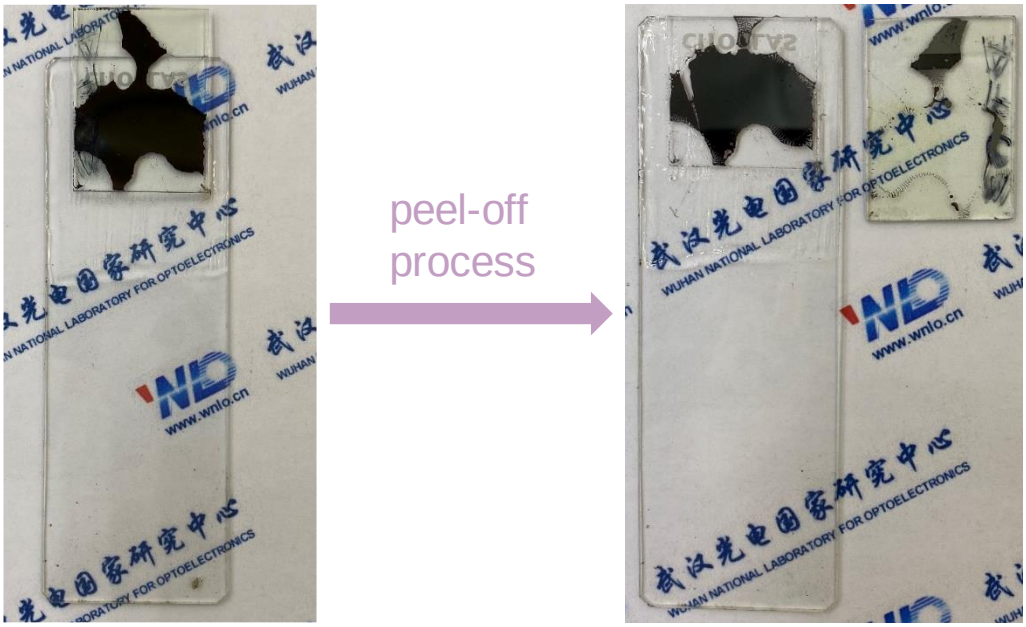

Supplementary Fig. 8. Peel-off method for the bottom surfaces of perovskite films. The bottom surface of perovskite films was fabricated through the following method: the top surface of the prepared perovskite film was partly pasted together with a glass slide using UV glue. After the glue was solidified overnight, the film was peeled off from the ITO substrate with force, and then the bottom surface of perovskite films for characterization was obtained.

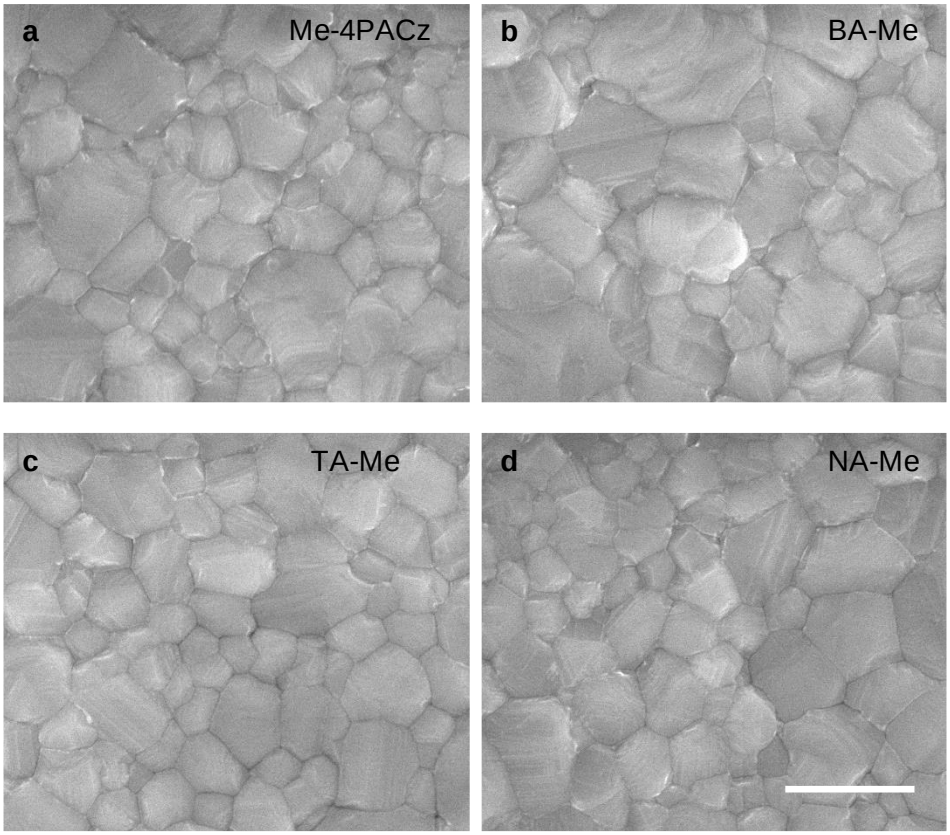

Supplementary Fig. 9. SEM images of top surfaces of perovskite films on (**a**) Me-4PACz, (**b**) BA-Me, (**c**) TA-Me, and (**d**) NA-Me SAMs. Scale bars, 1 μm.

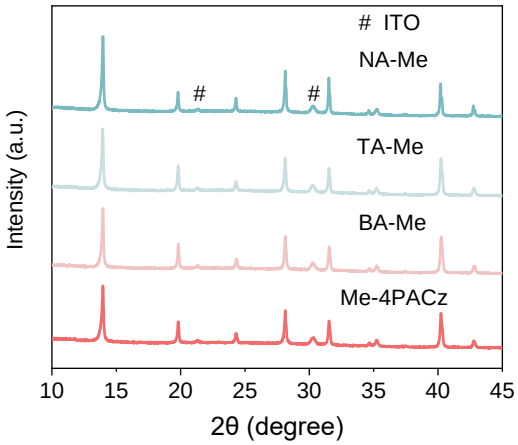

Supplementary Fig. 10. The X-ray diffraction (XRD) patterns of perovskite films on studied HSLs.

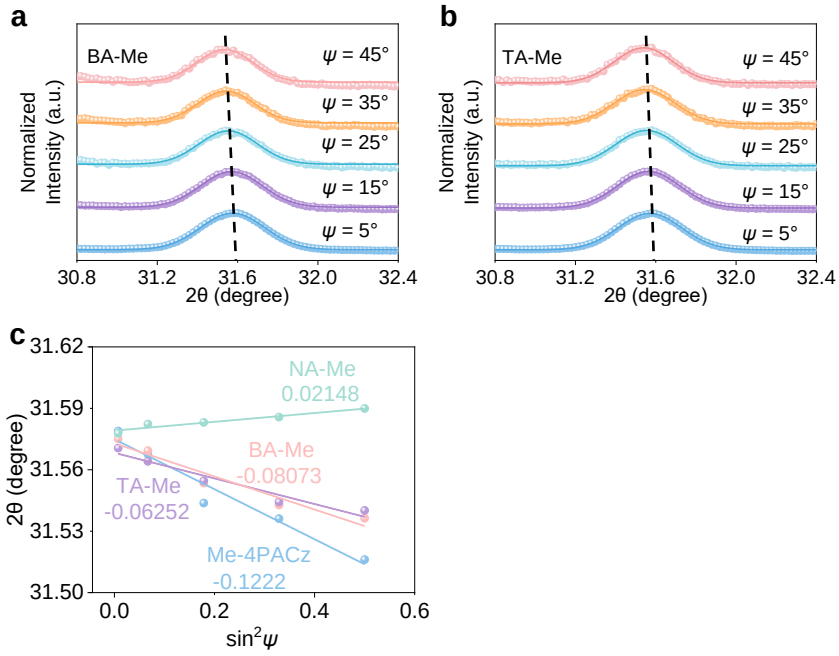

Supplementary Fig. 11. GIXRD characterization. **a-b**, GIXRD patterns measured at different ψ angles from 5° to 45° for perovskite films on (a) BA-Me and (b) TA-Me SAMs. **c**, The residual strain of the corresponding diffraction peaks (2θ) of perovskite films on studied HSL interlayers as a function of $\sin^2\psi$.

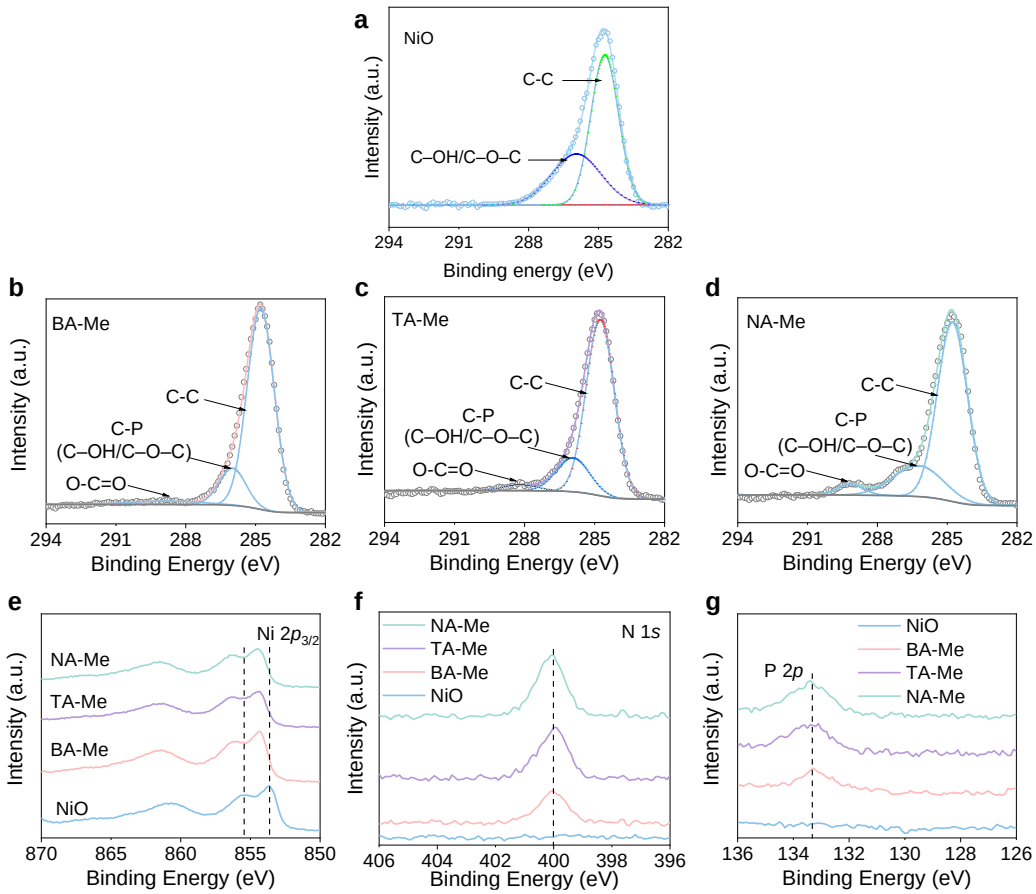

Supplementary Fig. 12. XPS characterization of mixed SAMs. **a-d**, High-resolution XPS spectra of C1*s* for films of (a) NiO, (b) BA-Me, (c) TA-Me, and (d) NA-Me. The purple line is attributed to C–OH/C–O–C contaminations for only NiO in C 1s spectra of NiO. The peak position corresponding to the original C–P bond should be attributed to C–P and C–OH/C–O–C contaminations for mixed SAMs deposited substrates. The presence of mixed SAMs was identified to successfully bond to the NiO substrate from the C 1*s* characterized peak of mixed SAMs, i.e., the O–C=O and C–P (C–OH/C–O–C contaminations) peaks located at the binding energies of approximately 289.2 eV and 286.3 eV, respectively. **e-g**, The XPS spectra of (e) Ni 2*p*, (f) N 1*s*, and (g) P 2*p* of NiO, BA-Me, TA-Me, and NA-Me films.

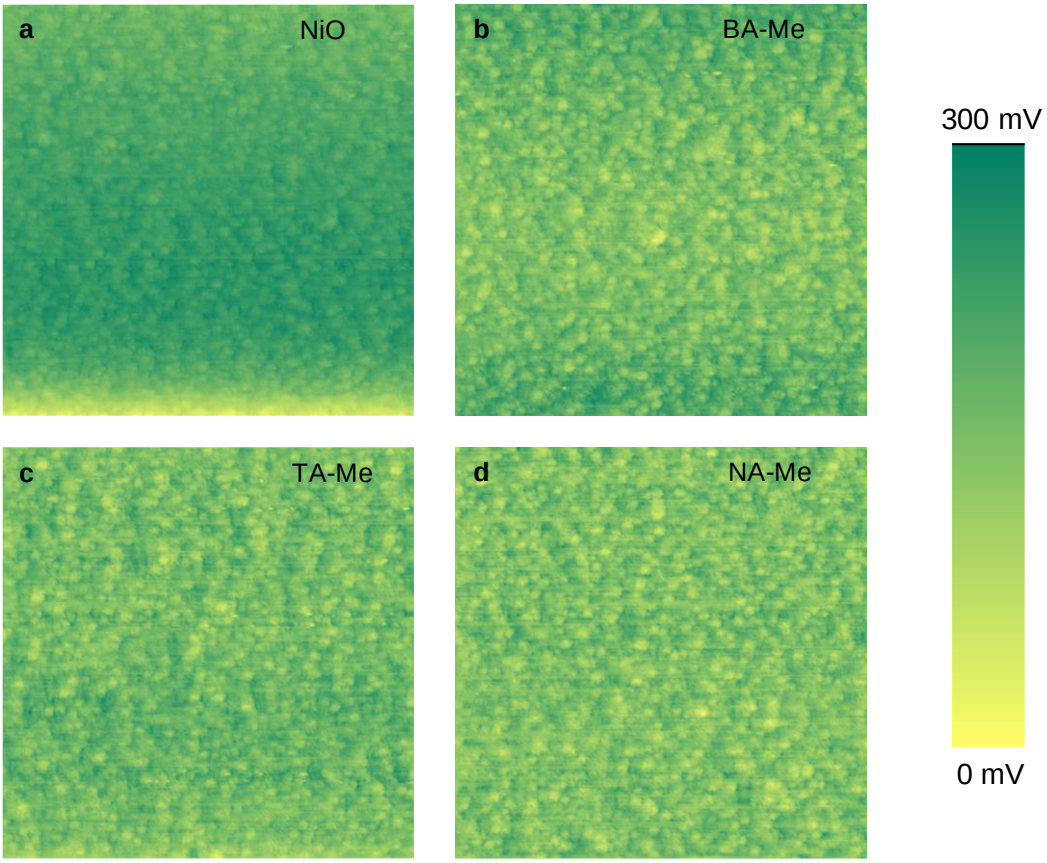

Supplementary Fig. 13. Surface CPD images for (**a**) bare NiO, (**b**) BA-Me-treated NiO, (**c**) TA-Me-treated NiO, and (**d**) NA-Me-treated NiO films derived from KPFM.

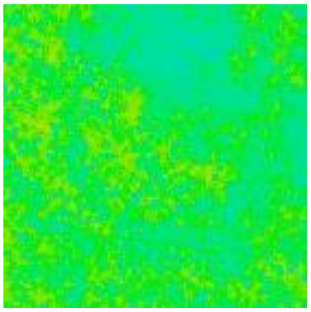

Supplementary Fig. 14. The FLIM of the exposed bottom surface of perovskite layers on BA-Me.

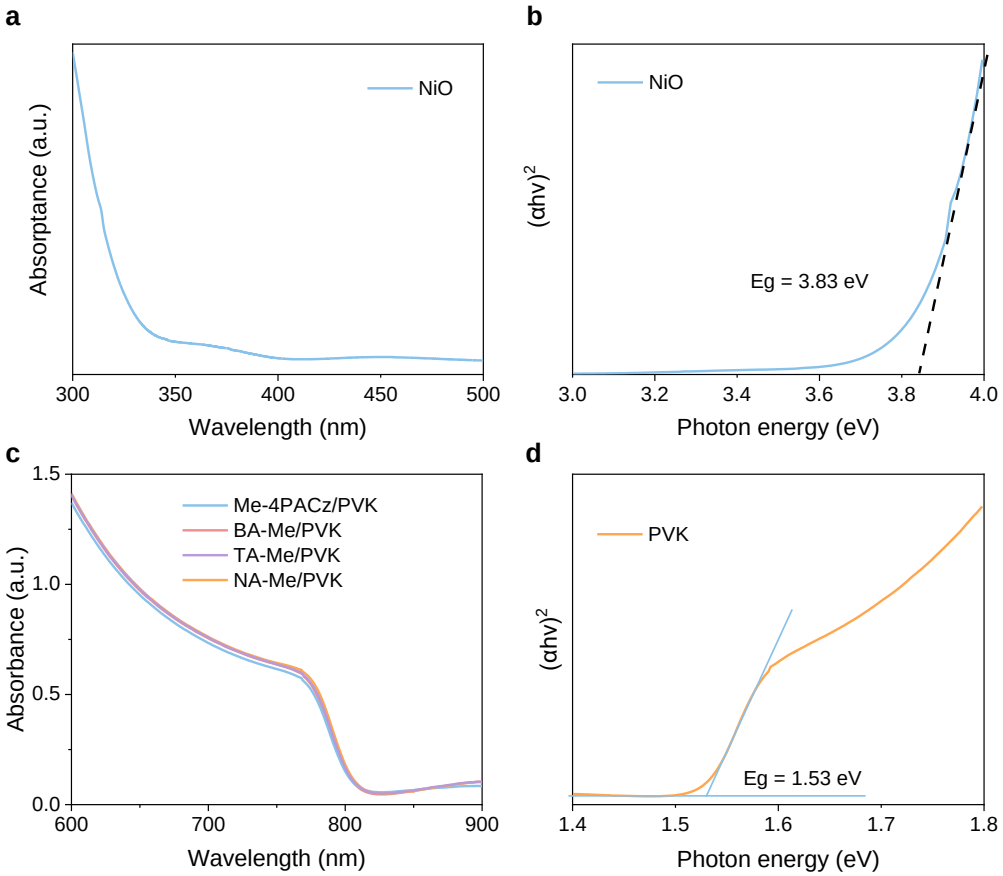

Supplementary Fig. 15. Ultraviolet-visible (UV-Vis) absorption spectra (**a** and **c**) and Tauc plots (**b** and **d**) of NiO and perovskite films.

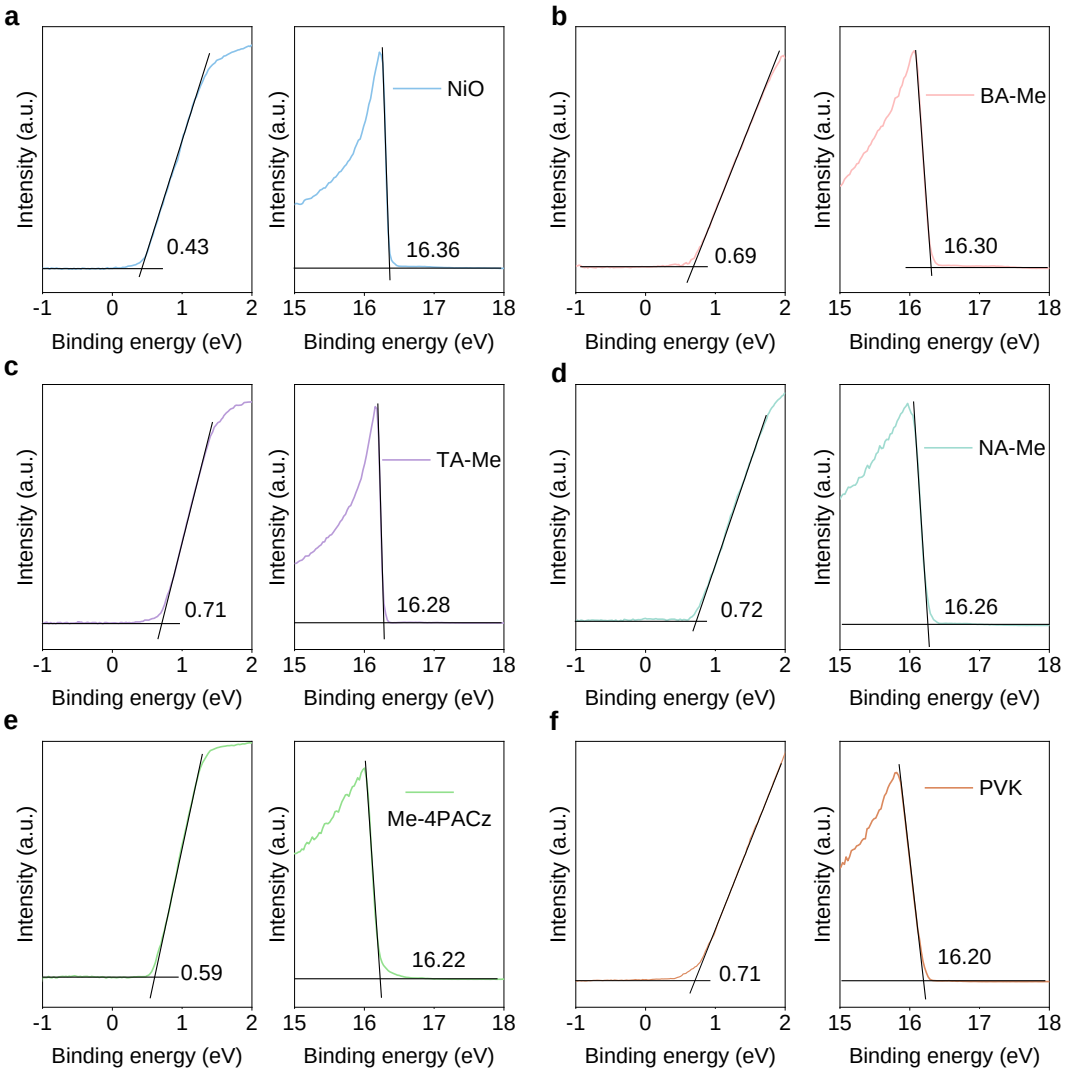

Supplementary Fig. 16. UPS spectra of (**a**) NiO, (**b**) BA-Me coated on NiO, (**c**) TA-Me coated on NiO, (**d**) NA-Me coated on NiO, (**e**) Me-4PACz coated on NiO, and (**e**) exposed bottom perovskite films deposited on ITO substrate, respectively.

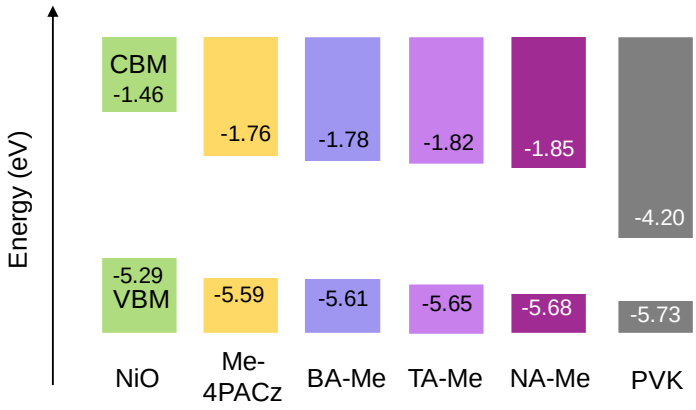

Supplementary Fig. 17. Schematic diagram of energy levels of VBM and conduction band minimum (CBM) derived from UPS spectra of the involved HSLs and the exposed bottom surface of the perovskite films.

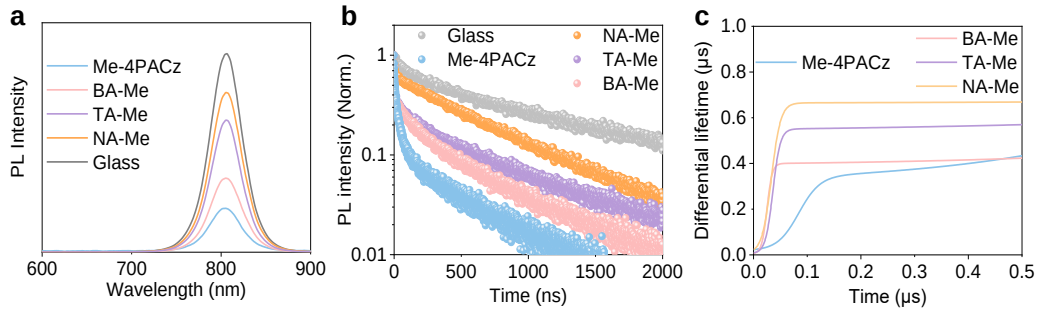

Supplementary Fig. 18. Steady-state PL spectra (**a**) and TRPL spectra (**b**) of perovskite films deposited on glass and different HSLs. (**c**) Differential lifetimes derived from fits to the transients in (c).

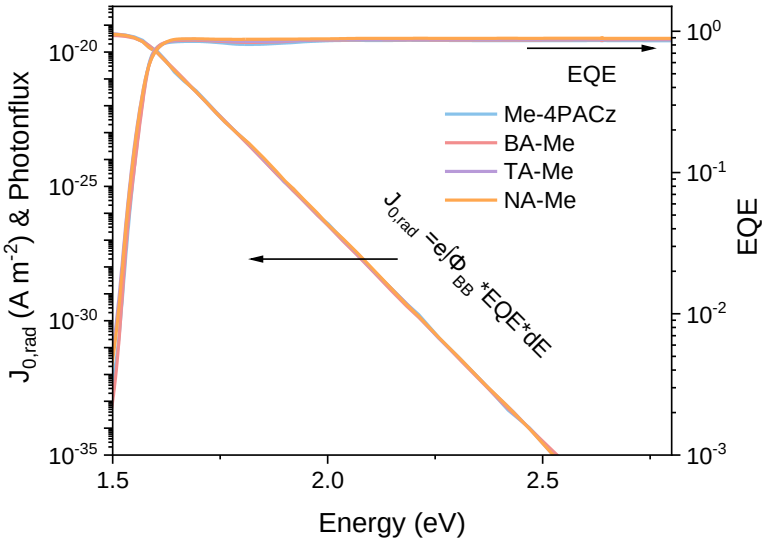

Supplementary Fig. 19. The highly sensitive EQE of the PSCs based on studied HSLs.

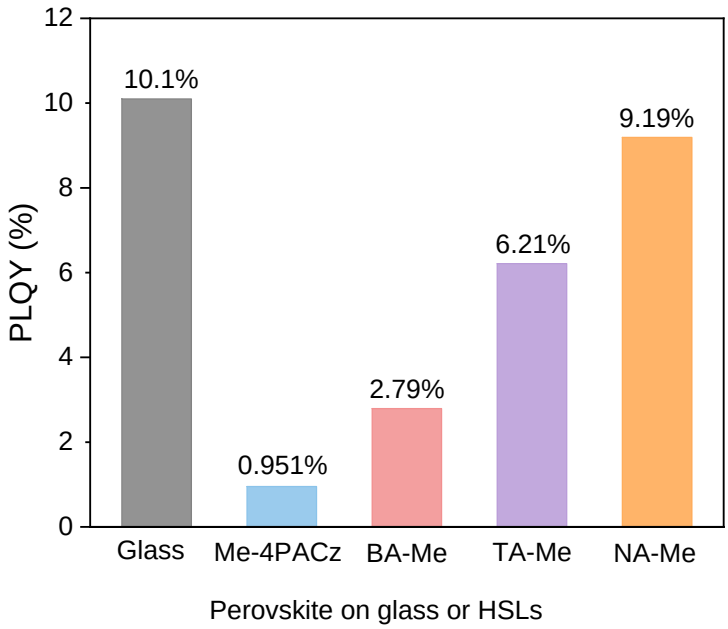

Supplementary Fig. 20. PLQY values of perovskite films on glass and involved HSLs.

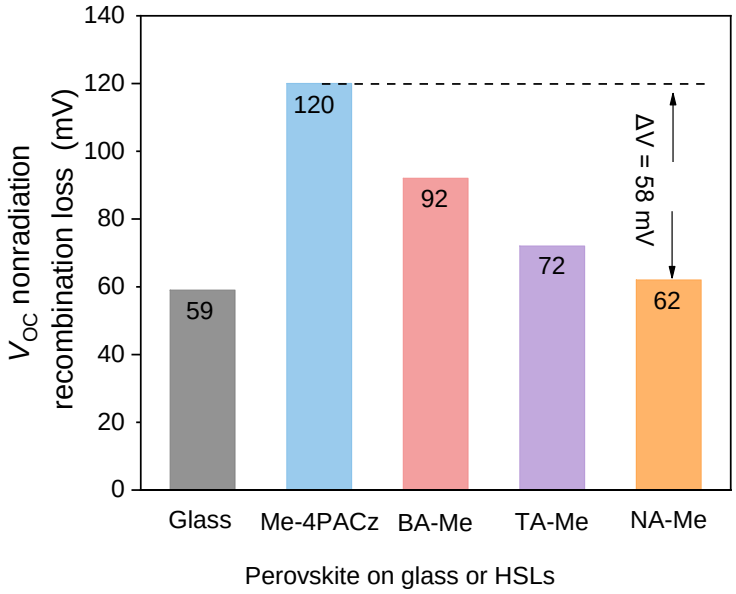

Supplementary Fig. 21. The calculated V_{OC} non-radiation recombination loss ($\Delta V_{OC}^{non-rad}$) values of perovskite films on glass and involved HSLs.

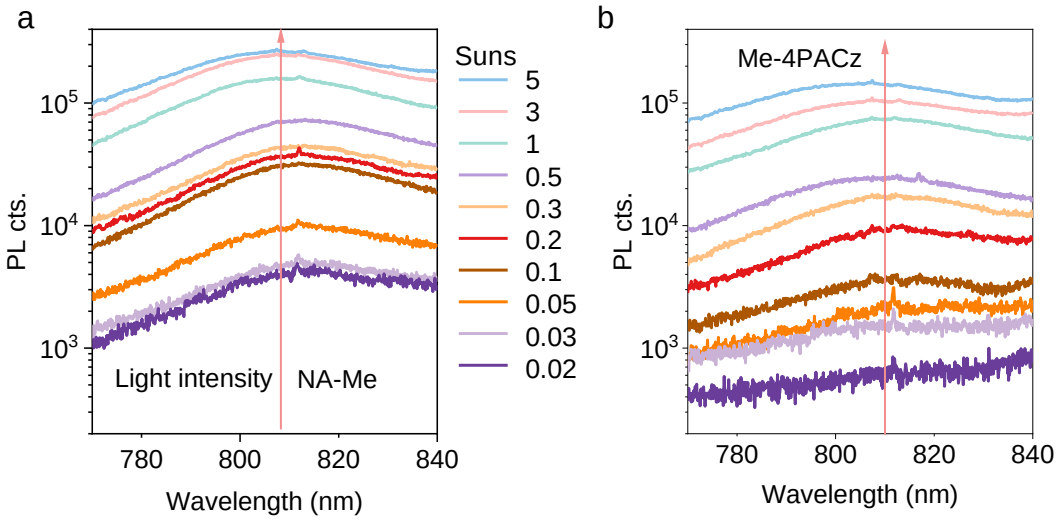

Supplementary Fig. 22. Absolute PL spectra of perovskite films on ITO/NiO/NA-Me (a) and Me-4PACz (b) under different incidence illumination intensities during the PLQY measurements.

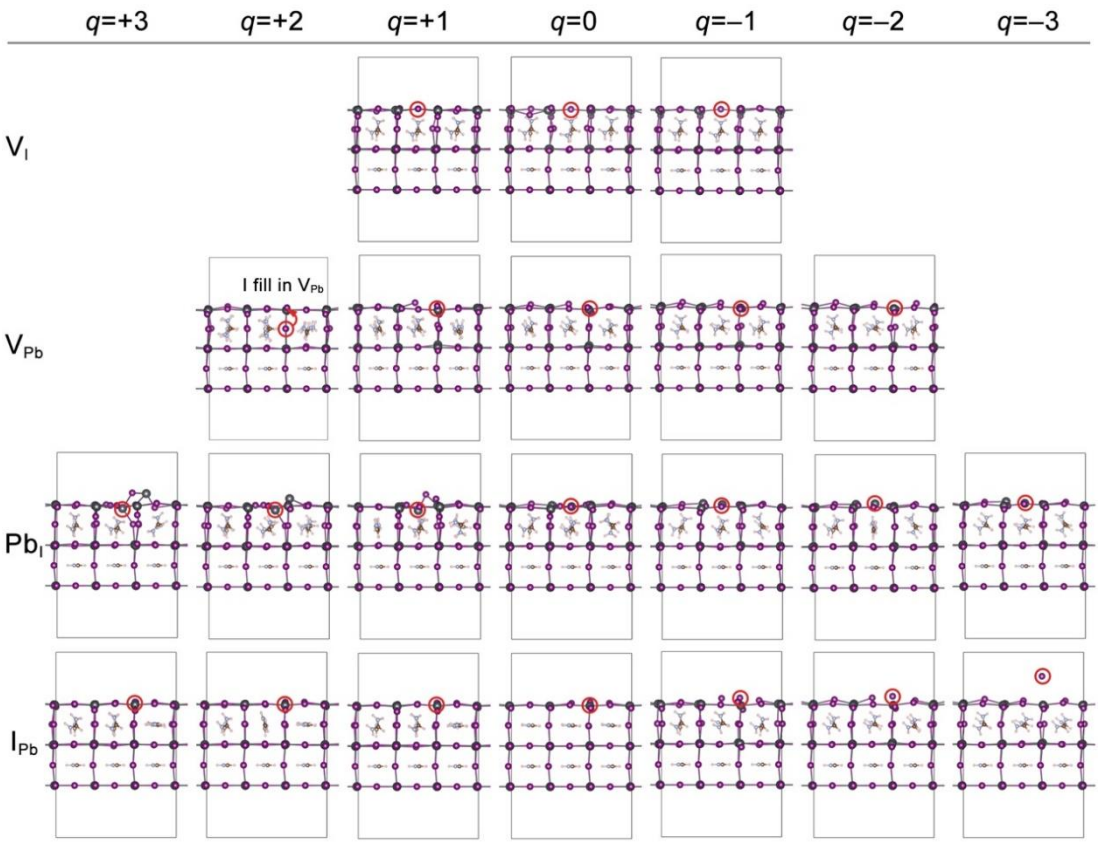

Supplementary Fig. 23. Optimized structures of the 3 × 3 × 2 perovskite slab with the neutral and charged V_I, V_{Pb}, Pb_I, and I_{Pb} surface defects. The red circles highlight the defect point. In the V_{Pb}^{2+} defect, the internal I atom moves to the surface to fill in the Pb-vacancy, leading to an I–Pb antisite with an I-vacancy defect.

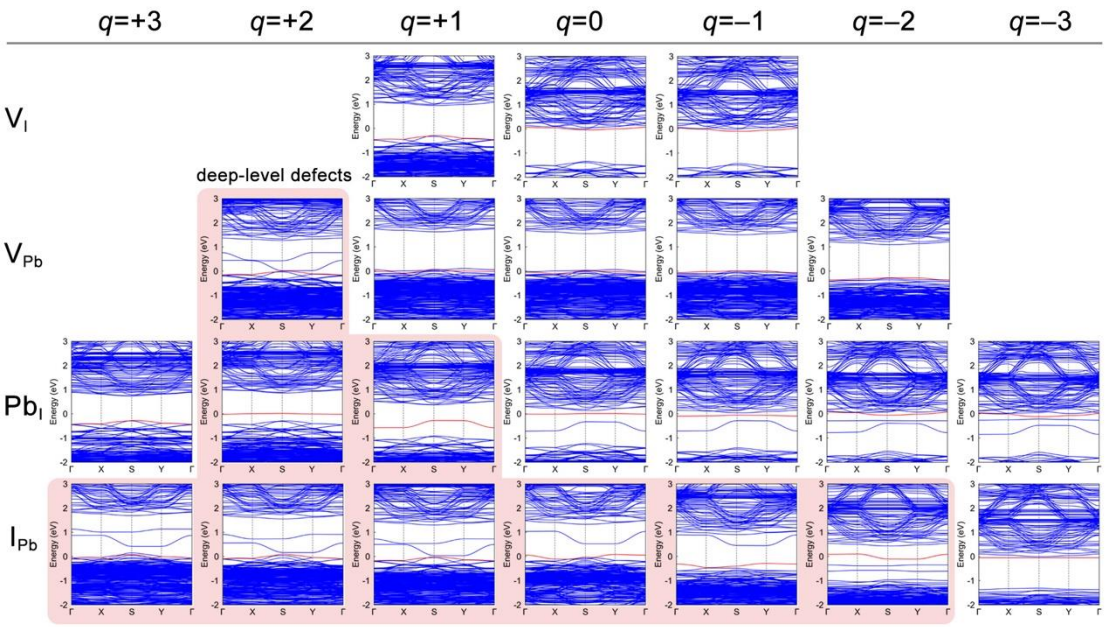

Supplementary Fig. 24. Band structures of the 3 × 3 × 2 perovskite slab with the neutral and charged V_I, V_{Pb}, Pb_I, and I_{Pb} surface defects. The red lines indicate the highest valence band.

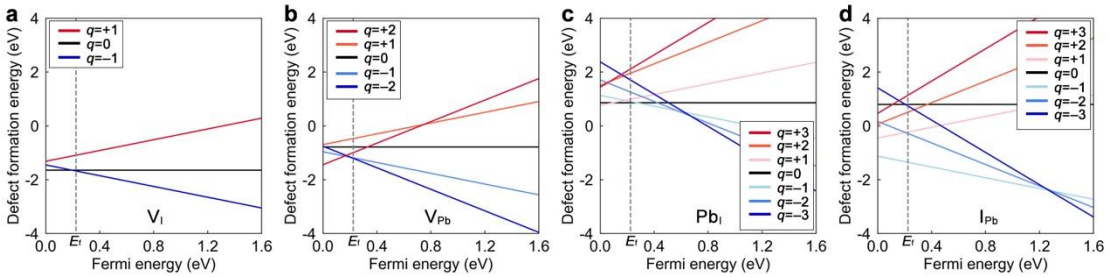

Supplementary Fig. 25. Defect transition level for the 3 × 3 × 2 perovskite with the (**a**) V_I, (**b**) V_{Pb}, (**c**) Pb_I, and (**d**) I_{Pb} surface defects with various point charges.

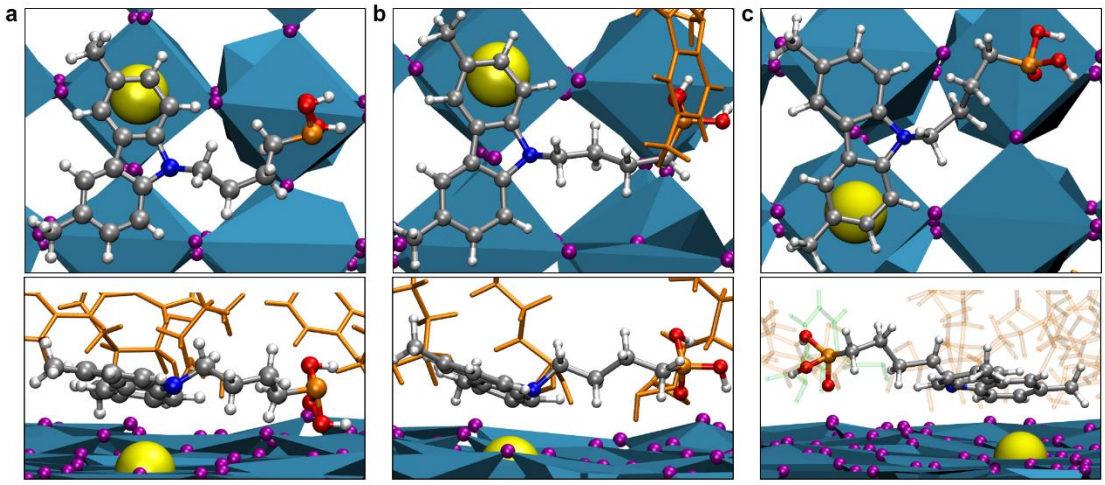

Supplementary Fig. 26. Top and side views for the molecular configuration of Me-4PACz adjacent to the V_{Pb}^{2+} defect in the molecular dynamics simulations for (a) pure Me-4PACz, (b) BA-Me, and (c) TA-Me hybrid systems.

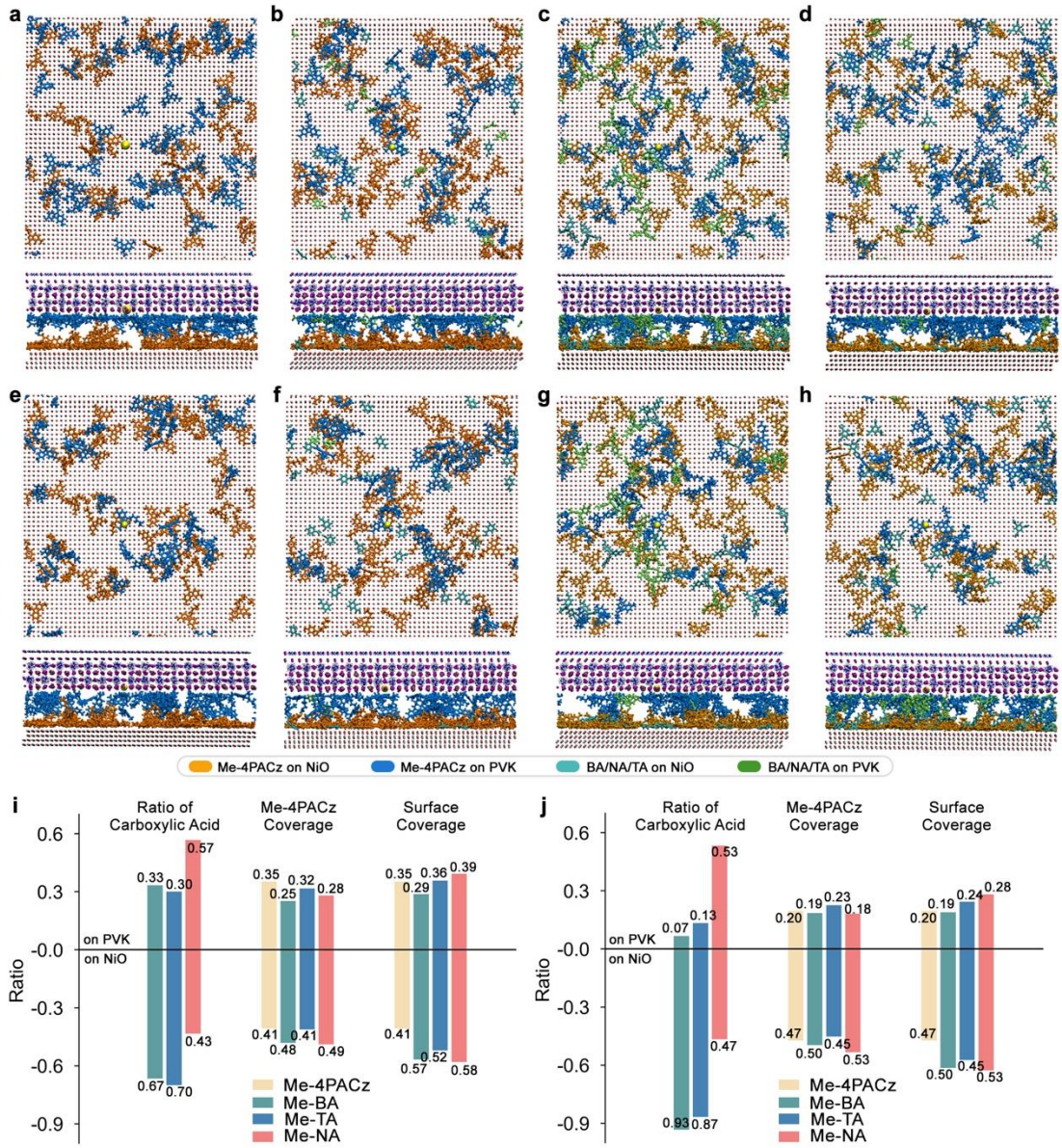

Supplementary Fig. 27. Top and side views of initial molecular representations for the heterojunctions containing a V_{Pb}^{2+} defect with only Me-4PACz (**a**), BA-Me (**b**), NA-Me (**c**), and TA-Me hybrid (**d**). The equilibrated molecular representations for the V_{Pb}^{2+} defective heterojunction models with only Me-4PACz (**e**), BA-Me (**f**), NA-Me (**g**), and TA-Me hybrid (**h**). Adsorption analysis for the perovskite and NiO surface in the (**i**) initial conditions and (**j**) equilibrated molecular configurations of the V_{Pb}^{2+} defective heterojunction models.

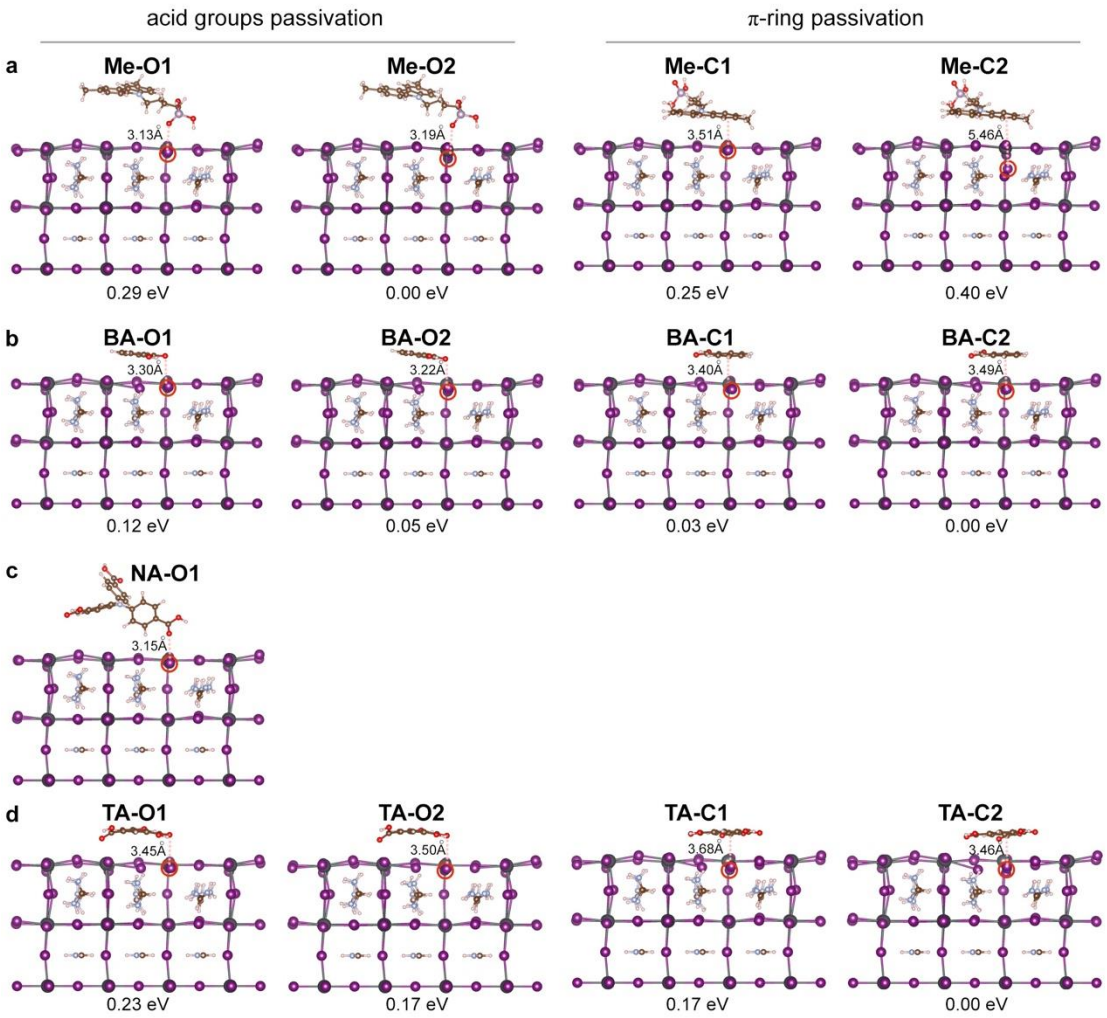

Supplementary Fig. 28. Optimized structures of the V_{Pb}^{2+} defective perovskite slab passivated with (**a**) Me-4PACz, (**b**) BA, (**c**) NA, and (**d**) TA. The molecular configurations of SAMs were sampled from MD simulations for the heterojunction models. The red circles highlight the defect points and the distance between SAMs and the defect are shown along with the structure. The relative energies to the lowest one are given below in each type of passivated structure. The Me-C2 structure shows a distance of 5.46 Å between Me-4PACz's π-ring and the internal I atoms. It suggests that Me-4PACz helps restore the internal Pb–I ionic bond. The passivated perovskite surface with Me-4PACz's π-ring is 0.40 eV higher than that with the phosphonic group. This energy difference (9.22 kcal mol^{-1}) can be compensated at room temperature, so the passivation is still thermally accessible.

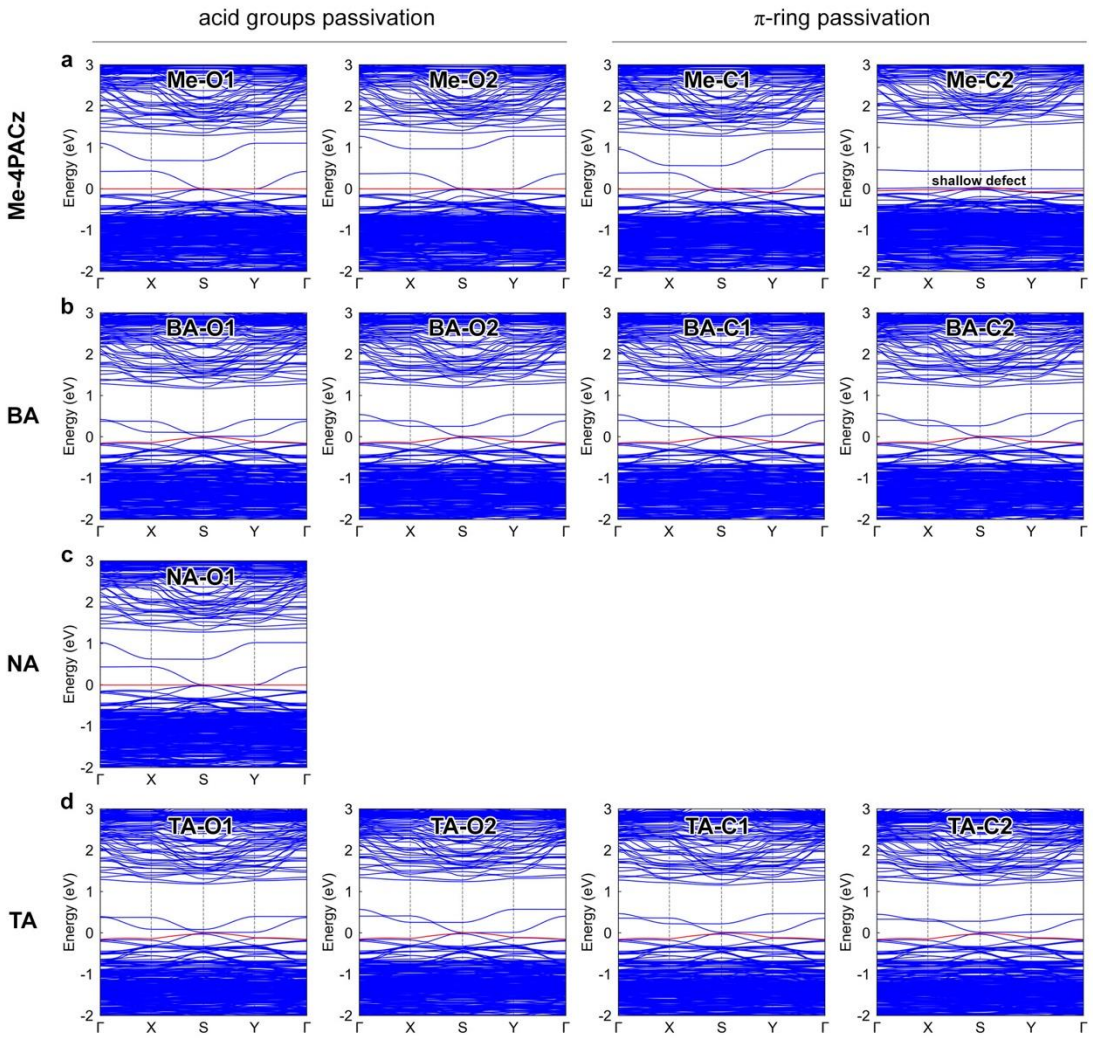

Supplementary Fig. 29. Band structures of the V_{Pb}^{2+} defective perovskite slab passivated with (**a**) Me-4PACz, (**b**) BA, (**c**) NA, and (**d**) TA. The red lines indicate the highest valence band.

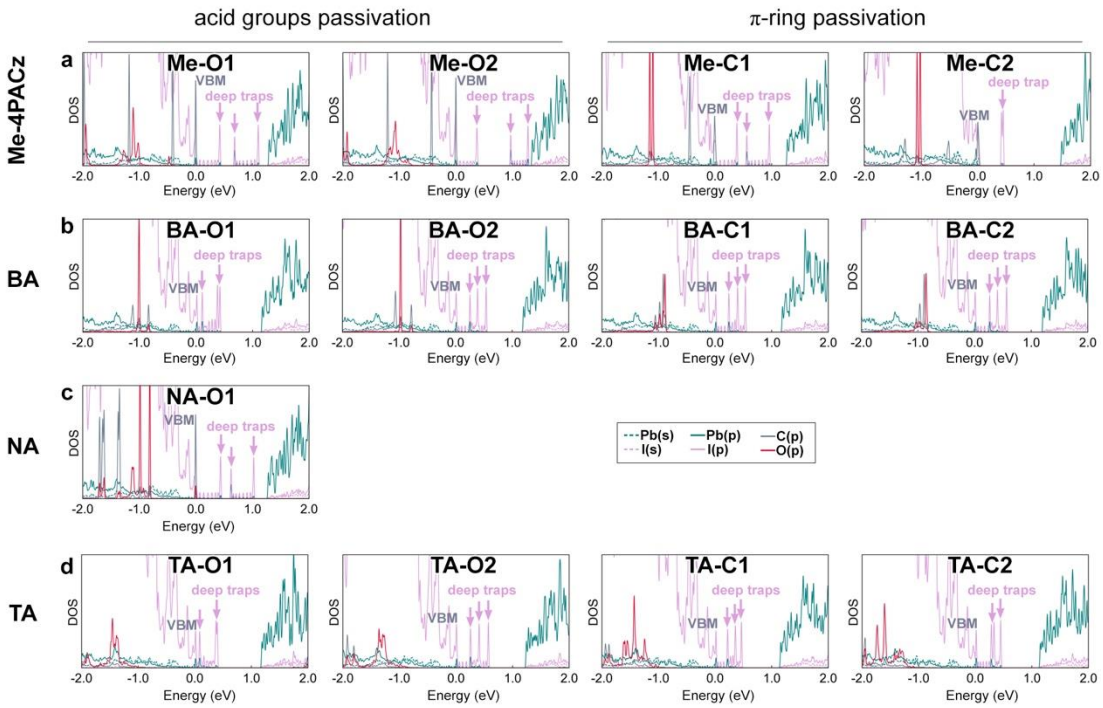

Supplementary Fig. 30. Projected density of states of the V_{Pb}^{2+} defective perovskite slab passivated with (**a**) Me-4PACz, (**b**) BA, (**c**) NA, and (**d**) TA.

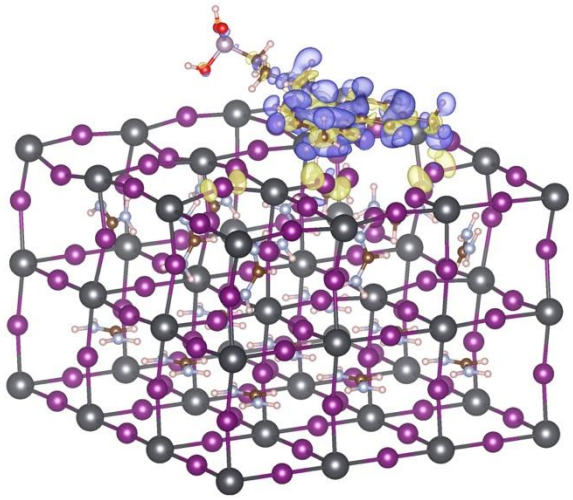

Supplementary Fig. 31. Differential charge density of the V_{Pb}^{2+} defective perovskite slab passivated by Me-4PACz's π-ring. Blue indicates the depletion of charge density; yellow represents the accumulation of charge density. Charge density transfer from blue to yellow.

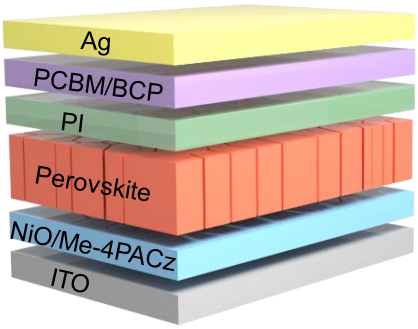

Supplementary Fig. 32. The structure of inverted PSCs in this work.

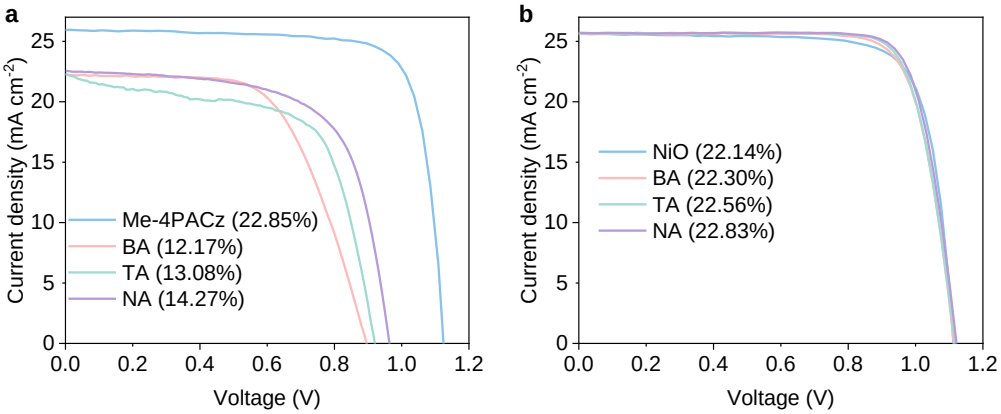

Supplementary Fig. 33. (a) *J–V* curves of PSCs based on four molecules acting as alone HSL layers (ITO/Me-4PACz (NA, TA, or BA)/perovskite/PI/PCBM/BCP/Ag). (b) *J–V* curves of PSCs with the configuration of ITO/NiO/BA (TA or NA)/perovskite/PI/PCBM/BCP/Ag.

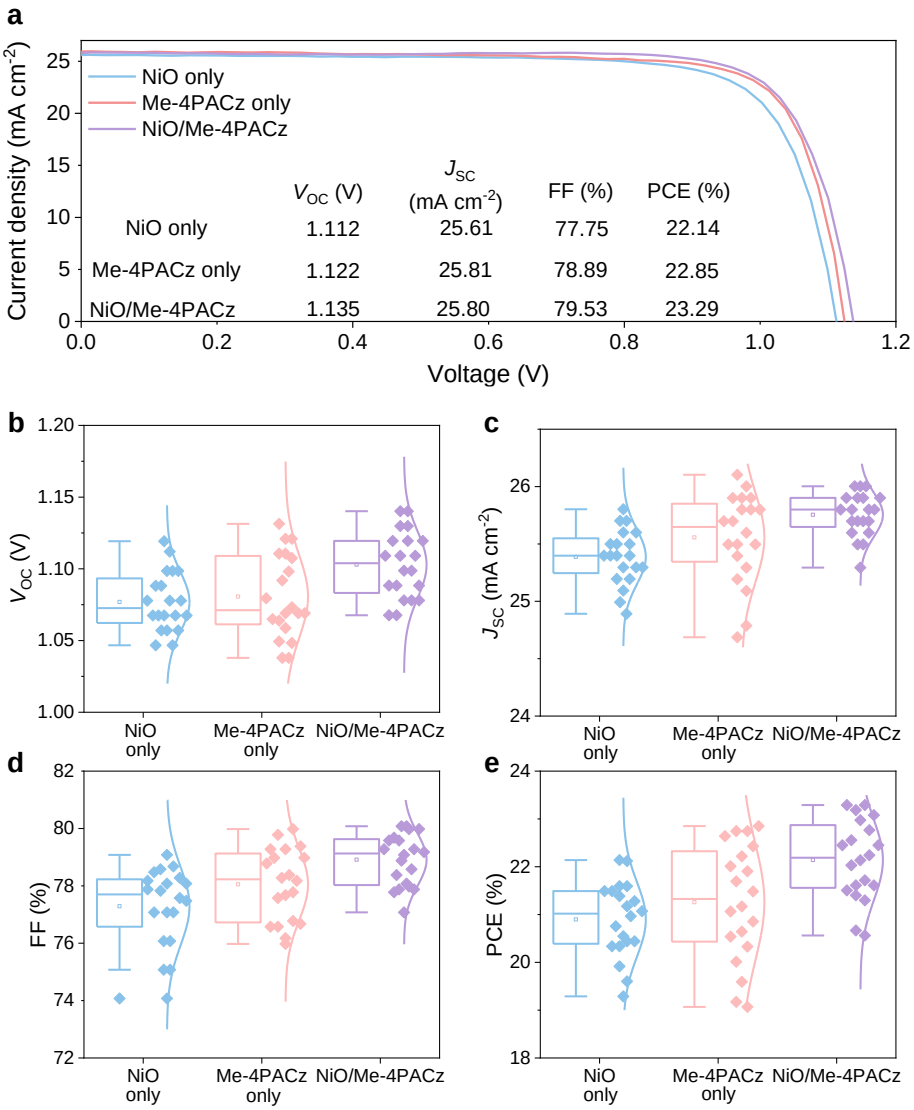

Supplementary Fig. 34. Photovoltaic performances based on different HSLs. **a**, *J*–*V* curves of PSCs with different HSLs under reverse scan direction. **b-e**, Statistical photovoltaic parameters of (b) V_{OC}, (c) J_{SC}, (d) FF, and (e) PCE of the PSCs using single HSL of NiO and Me-4PACz and bilayer HSLs of NiO/Me-4PACz (20 devices for each type).

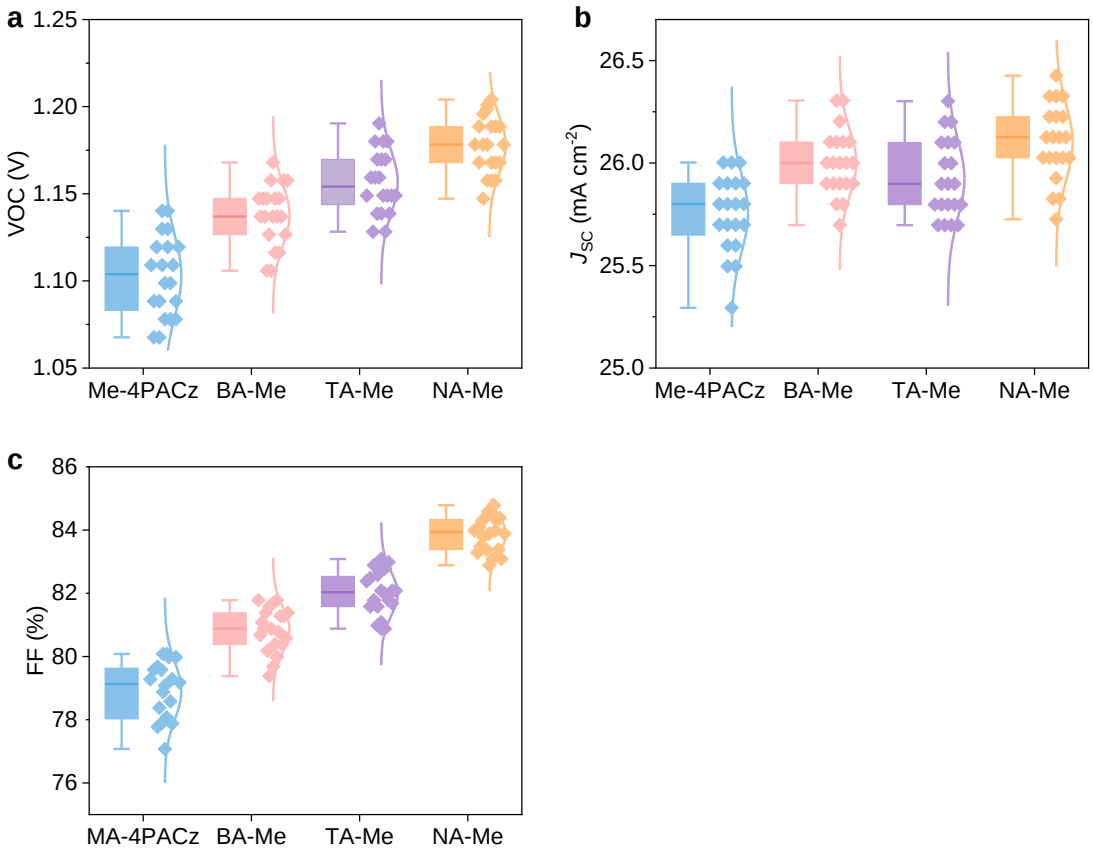

Supplementary Fig. 35. Statistical photovoltaic parameters of the PSCs using Me-4PACz and mixed SAMs. **a**, V_{OC}. **b**, J_{SC}. **c**, FF (20 devices for each type).

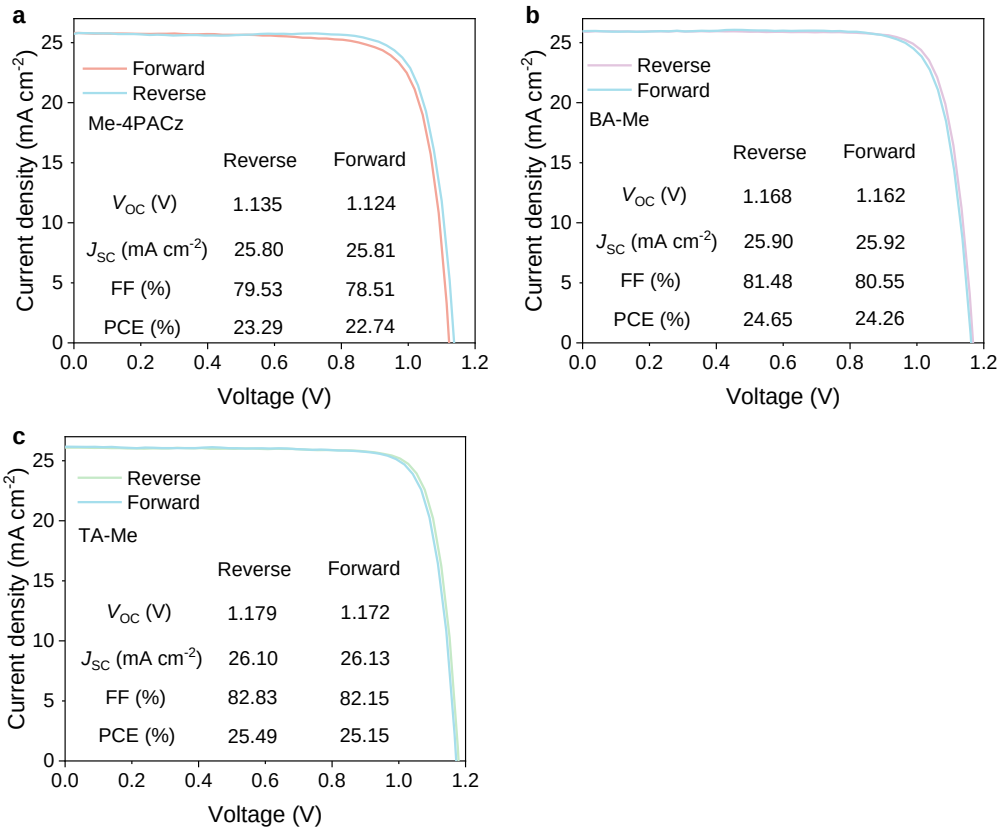

Supplementary Fig. 36. *J–V* curves of the champion devices based on different HSLs under reverse and forward scans. **a**, Me-4PACz. **b**, BA-Me. **c**, TA-Me.

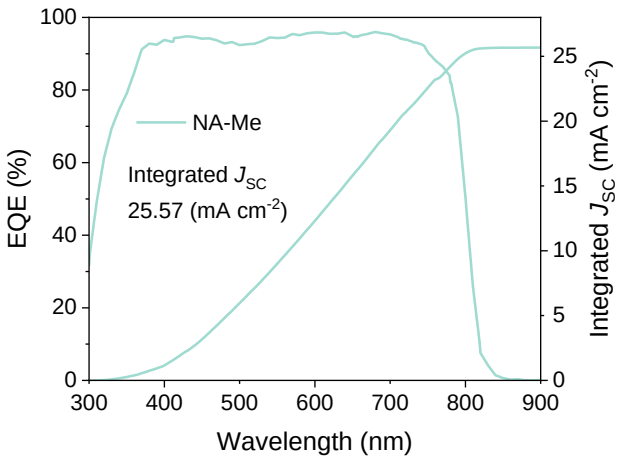

Supplementary Fig. 37. EQE curve of the champion inverted PSC based on the NA-Me.

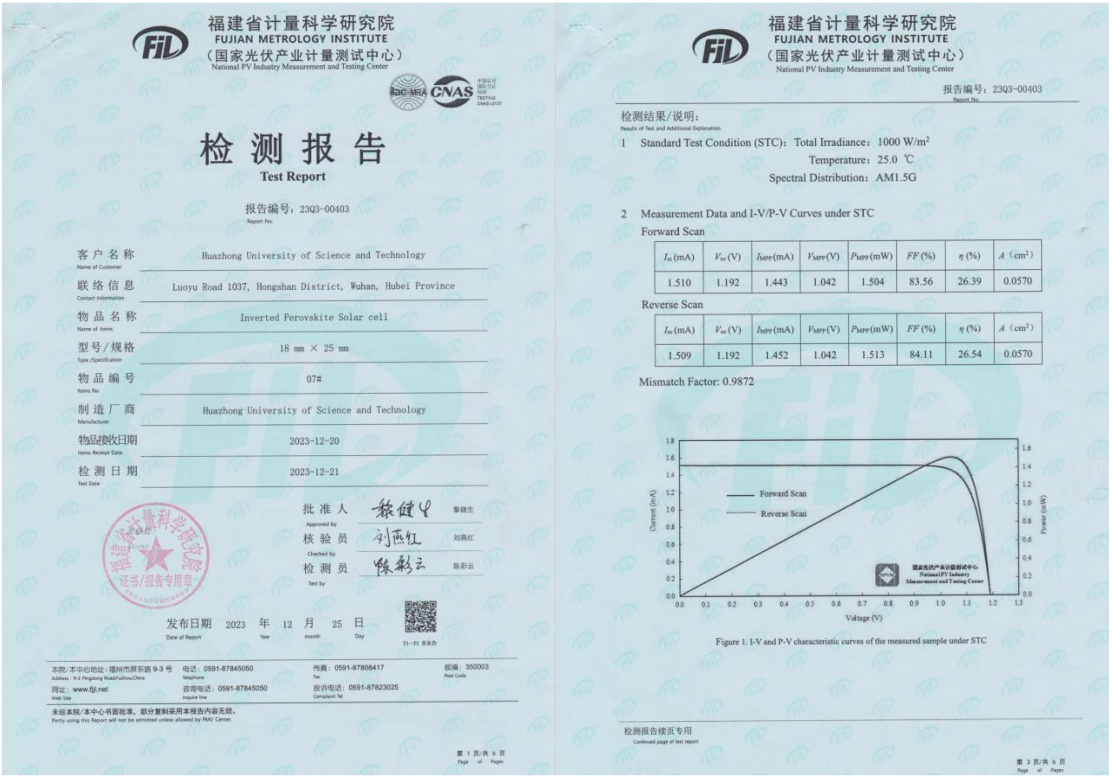

福建省计量科学研究院
FUJIAN METROLOGY INSTITUTE
（国家光伏产业计量测试中心）
National PV Industry Measurement and Testing Center

检 测 报 告
Test Report

报告编号：23Q3-00403

客户名称 Name of Customer	Huazhong University of Science and Technology
联络信息 Contact Information	Luoyu Road 1037, Hongshan District, Wuhan, Hubei Province
物品名称 Name of Items	Inverted Perovskite Solar cell
型号/规格 Type /Specification	18 mm × 25 mm
物品编号 Items No	07#
制造厂商 Manufacturer	Huazhong University of Science and Technology
物品接收日期 Items Receipt Date	2023-12-20
检测日期 Test Date	2023-12-21

批准人 Approved by 黎健华
核验员 Checked by 刘燕红
检测员 Test by 陈彩云

发布日期 Date of Report 2023 年 Year 12 月 month 25 日 Day

本院/本中心地址：福州市屏东路 9-3 号 Address：9-3 Pingdong Road Fuzhou China 电话：0591-87845050 Telephone 传真：0591-87808417 Fax 邮编：350003 Post Code
网址：www.fjjl.net Web Site 咨询电话：0591-87845050 Inquire line 投诉电话：0591-87823025 Complaint Tel

未经本院/本中心书面批准，部分复制采用本报告内容无效。
Partly using this Report will not be admitted unless allowed by FMU Center.

第 1 页/共 6 页 Page of Pages

福建省计量科学研究院
FUJIAN METROLOGY INSTITUTE
（国家光伏产业计量测试中心）
National PV Industry Measurement and Testing Center

报告编号：23Q3-00403 Report No.

检测结果/说明：
Results of Test and Additional Explanation.

1 Standard Test Condition (STC)：Total Irradiance：1000 W/m²
Temperature：25.0 ℃
Spectral Distribution：AM1.5G

2 Measurement Data and I-V/P-V Curves under STC

Forward Scan

I_{sc} (mA)	V_{oc} (V)	I_{MPP} (mA)	V_{MPP} (V)	P_{MPP} (mW)	FF (%)	η (%)	A (cm²)
1.510	1.192	1.443	1.042	1.504	83.56	26.39	0.0570

Reverse Scan

I_{sc} (mA)	V_{oc} (V)	I_{MPP} (mA)	V_{MPP} (V)	P_{MPP} (mW)	FF (%)	η (%)	A (cm²)
1.509	1.192	1.452	1.042	1.513	84.11	26.54	0.0570

Mismatch Factor: 0.9872

Figure 1. I-V and P-V characteristic curves of the measured sample under STC

检测报告续页专用
Continued page of test report

第 3 页/共 6 页 Page of Pages

Supplementary Fig. 38. The certificate of one NA-Me inverted device (*J–V* characterization). The report is issued by NPVM (Chinese National PV Industry Measurement and Testing Center). The aperture area is 0.057 cm^2 measured by NPVM. The report includes the optical aperture area, *J–V*, MPPT, and EQE measurements.

福建省计量科学研究院
FUJIAN METROLOGY INSTITUTE
（国家光伏产业计量测试中心）
National PV Industry Measurement and Testing Center

报告编号：23Q3-00403

检测结果/说明：

3 Measurement Data and Curves for MPPT under STC

η (%)	26.54
P_{MPP} (mW)	1.513
I_{MPP} (mA)	1.452
V_{MPP} (V)	1.042

Note: Measurement data for MPPT under STC in the above table was the mean value acquired during the final 30 seconds of the 300 seconds test

Figure 2. Measurement curves of the measured sample for MPPT

检测报告续页专用

福建省计量科学研究院
FUJIAN METROLOGY INSTITUTE
（国家光伏产业计量测试中心）
National PV Industry Measurement and Testing Center

报告编号：23Q3-00409

检测结果/说明：

Figure 1. Relative spectral responsivity curve of the measured sample

Relative Spectral Responsivity:
(300~400) nm: U_{rel} = 2.2% (k=2); (400~900) nm: U_{rel} = 1.8% (k=2).

Testing Method (Code and Name) for This Test
IEC 60904-8: 2014 Photovoltaic devices- Part 8: Measurement of spectral responsivity of a photovoltaic (PV) device

Measurement Standards Used in This Test

Name	Number	Measuring Range	Uncertainty or Accuracy Class or Maximum Permissible Error	Name of Traceability Institution/Certificate No.	Due Date
Si Photoelectric Detector	Si-2	(200~1100) nm	U_{rel}=19.0%~6.9% (k=2) (200~230)nm ;U_{rel}=6.9%~3.7% (k=2) (230~240)nm ; U_{rel}=3.7%~1.8% (k=2) (240~300)nm ; U_{rel}=1.8%~1.7% (k=2) (300~400)nm ; U_{rel}=1.7%~1.3% (k=2) (400~450)nm ;U_{rel}=1.3%~1.2% (k=2)(450~1000)nm ; U_{rel}=1.2%~1.7% (k=2) (1000~1100)nm	National Institute of Metrology, China/ GXgf2023-00265	2025-02-01

以下空白
Blank below

检测报告续页专用

Supplementary Fig. 39. The certificate of one NA-Me inverted device (steady-state PCE characterization). The report is issued by NPVM. The stabilized PCE of 26.54% is determined from MPPT for 300 s.

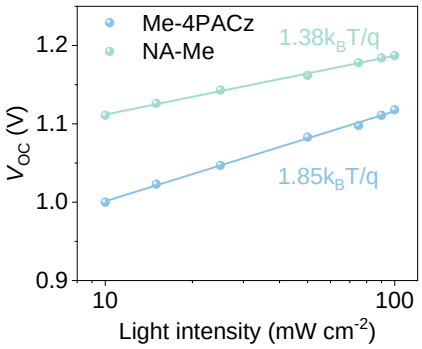

Supplementary Fig. 40. Light intensity dependence of V_{OC} on the PSCs with NA-Me or Me-4PACz.

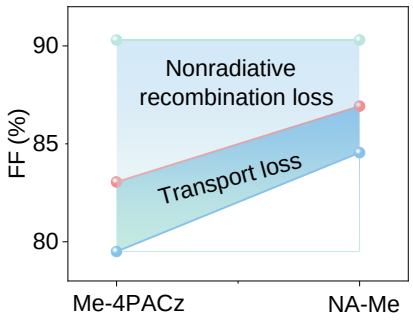

Supplementary Fig. 41. Detailed FF loss analysis of the inverted PSCs with NA-Me and Me-4PACz.

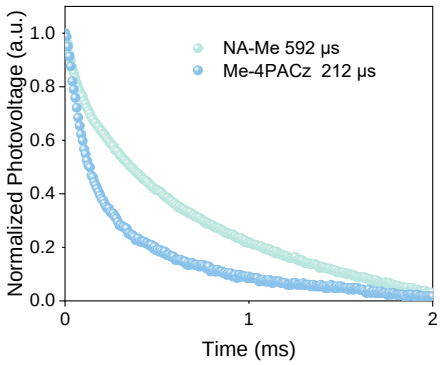

Supplementary Fig. 42. Transient photovoltage (TPV) plots of the devices with NA-Me or Me-4PACz.

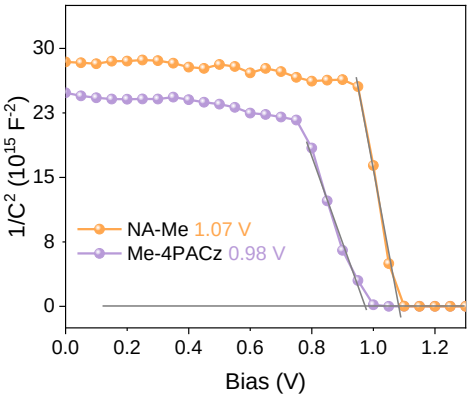

Supplementary Fig. 43. Mott-Schottky plots for devices with studied SAMs. The curves on top of the data were extracted by linear fitting the drop region of Mott-Schottky plots, and V_{bi} was obtained via the intercept of the straight line with the χ axis.

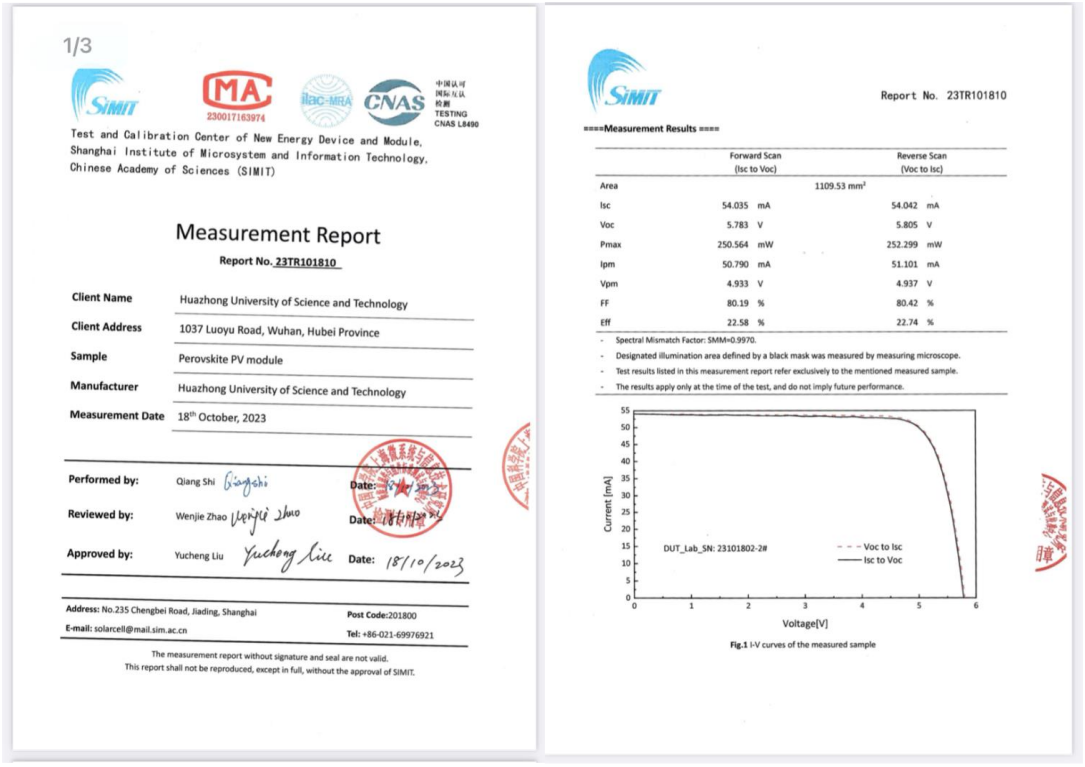

1/3

SIMIT MA 230017163974 ilac-MRA CNAS 中国认可 国际互认 检测 TESTING CNAS L8490

Test and Calibration Center of New Energy Device and Module,
Shanghai Institute of Microsystem and Information Technology,
Chinese Academy of Sciences (SIMIT)

Measurement Report

Report No. 23TR101810

Client Name	Huazhong University of Science and Technology
Client Address	1037 Luoyu Road, Wuhan, Hubei Province
Sample	Perovskite PV module
Manufacturer	Huazhong University of Science and Technology
Measurement Date	18th October, 2023

Performed by: Qiang Shi Date:

Reviewed by: Wenjie Zhao Date:

Approved by: Yucheng Liu Date: 18/10/2023

Address: No.235 Chengbei Road, Jiading, Shanghai Post Code:201800
E-mail: solarcell@mail.sim.ac.cn Tel: +86-021-69976921

The measurement report without signature and seal are not valid.
This report shall not be reproduced, except in full, without the approval of SIMIT.

SIMIT Report No. 23TR101810

====Measurement Results ====

	Forward Scan (Isc to Voc)	Reverse Scan (Voc to Isc)
Area	1109.53 mm²	
Isc	54.035 mA	54.042 mA
Voc	5.783 V	5.805 V
Pmax	250.564 mW	252.299 mW
Ipm	50.790 mA	51.101 mA
Vpm	4.933 V	4.937 V
FF	80.19 %	80.42 %
Eff	22.58 %	22.74 %

- Spectral Mismatch Factor: SMM=0.9970.
- Designated illumination area defined by a black mask was measured by measuring microscope.
- Test results listed in this measurement report refer exclusively to the mentioned measured sample.
- The results apply only at the time of the test, and do not imply future performance.

Fig.1 I-V curves of the measured sample

Supplementary Fig. 44. Certified performance of inverted mini-modules with an aperture area of 11.1 cm^2 based on NA-Me. The certified efficiency is 22.74% under reverse scan with a high FF of 80.42% along with a low hysteresis (22.58% under forward scan).

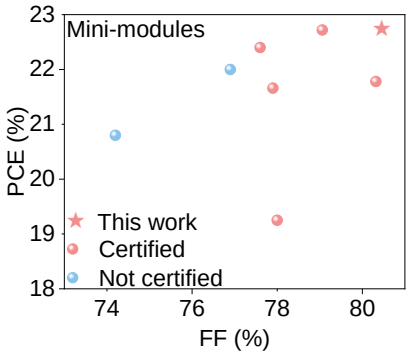

Supplementary Fig. 45. Comparison of the PCE and FF of our mini-modules with other reported high-performance modules.

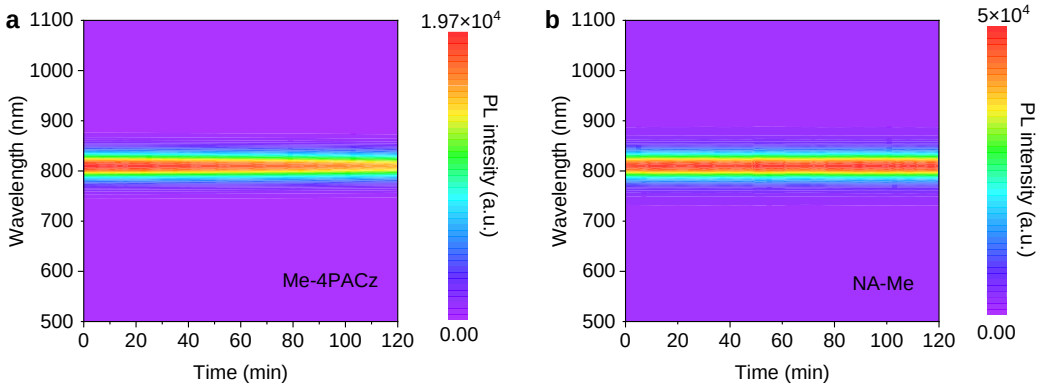

Supplementary Fig. 46. In-situ PL spectra of perovskite films deposited on (**a**) Me-4PACz and (**b**) NA-Me SAMs under continuous laser irradiation in air ambient for different durations (0-120 min) with a recorded temperature of 85 °C.

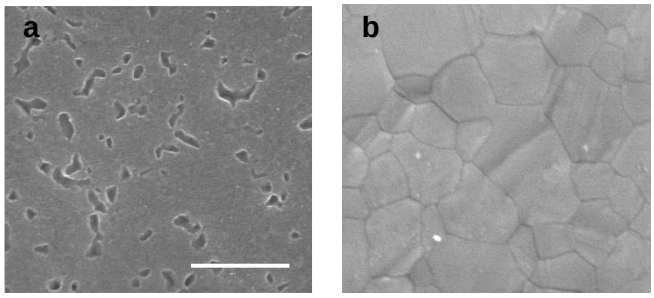

Supplementary Fig. 47. SEM images of the bottom surface of perovskite films on Me-4PACz (**a**) and NA-Me (**b**) after continuous laser irradiation for 120 min at 85 °C. Scale bars, 1 μm.

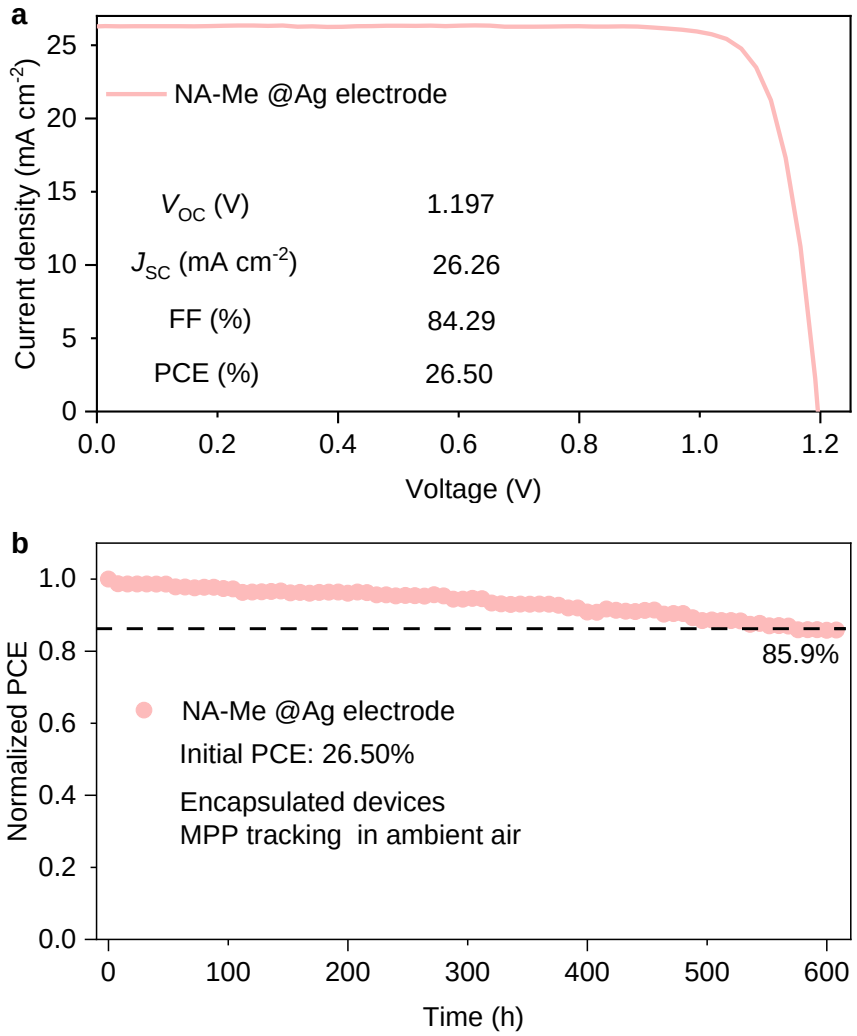

Supplementary Fig. 48. a, *J–V* curve of the NA-Me device with Ag electrode used for operational stability test. **b**, Operational stability of the corresponding device under continuous 1-sun equivalent white-light LED illumination with MPPT at 65 °C in ambient air. The NA-Me device with the Ag electrode exhibited inferior stability, which only retained 85.9% of its initial PCE (26.50%) after over 600 hours.

Supplementary Fig. 49. The photographs of the damp-heat chamber in our lab. The temperature and relative humidity levels were maintained at 85 °C and 85% RH, respectively, following the IEC 61215:2016 standard.

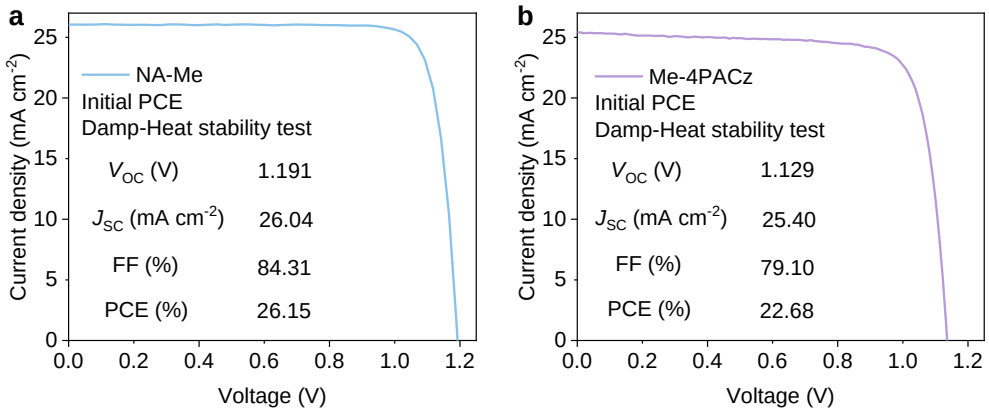

Supplementary Fig. 50. *J–V* curves of the representative NA-Me (**a**) and Me-4PACz (**b**) devices used in the damp heat stability test.

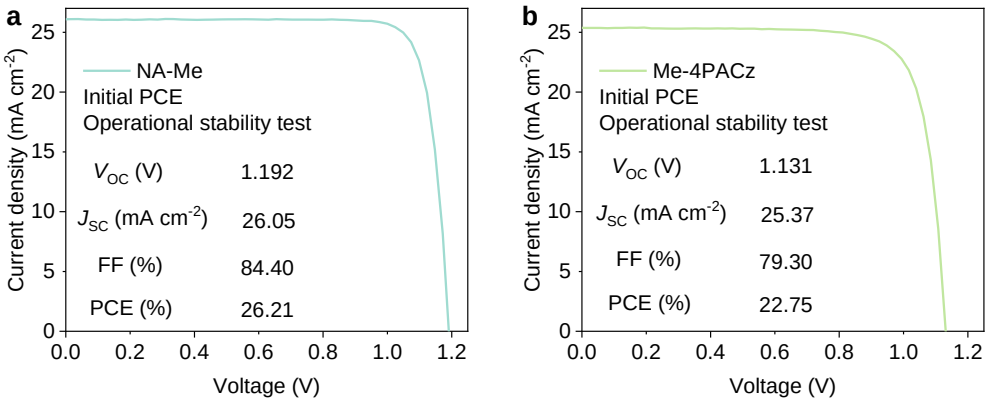

Supplementary Fig. 51. *J–V* curves of the NA-Me (**a**) and Me-4PACz (**b**) devices used in the operational stability test.

Supplementary Table 1. Binding energies of Me-4PACz, BA-Me, NA-Me, and TA-Me were computed with the PBE0+DFTD3 and optB88-vdW approach.

Dimers	PBE+D3 (eV)	optB88-vdW (eV)
Me-4PACz[a]	–0.17	–0.31
BA-Me[b]	–0.35	–0.47
NA-Me[b]	–0.61	–0.68
TA-Me[b]	–0.48	–0.62

[a]Geometries were optimized according to each method. [b]Geometries were optimized with the PBE+DFTD3 approach.

Supplementary Table 2. Electronic parameters of the perovskite film and different HSLs extracted from UPS spectra. PVK: exposed bottom surface of the perovskite film.

Condition	E_{cutoff} (eV)	E_{onset} (eV)	VBM (eV)	Eg (eV)	CBM (eV)
NiO	16.36	0.43	–5.29	3.83	–1.46
BA-Me	16.30	0.69	–5.61	3.83	–1.78
TA-Me	16.28	0.71	–5.65	3.83	–1.82
NA-Me	16.26	0.72	–5.68	3.83	–1.85
Me-4PACz	16.22	0.59	–5.59	3.83	–1.76
PVK	16.20	0.71	–5.74	1.53	–4.20

Supplementary Table 3. The PL decay fitting parameters of perovskite film and SAMs/perovskite junctions.

Samples	A_1	τ_1 (ns)	A_2	τ_2 (ns)	τ_{ave} (ns)
Me-4PACz	0.536	18.6	0.130	310.1	75.5
BA-Me	0.605	4.81	0.290	389.8	129.6
TA-Me	0.593	6.81	0.276	593.6	193.2
NA-Me	0.347	8.56	0.584	661.3	418.0
Glass	0.381	185.7	0.511	1455.5	913.1

The average carrier lifetime (τ_{ave}) was calculated according to the equation:

$$\tau_{ave} = \frac{A_1\tau_1 + A_2\tau_2}{A_1 + A_2}$$

Supplementary Table 4. The fitting parameters of the two-trap level SRH model.

Sample	Me-4PACz	NA-Me
k_{tr} ($\times 10^6$ s^{-1})	8.0	3.2
k_{deep} ($\times 10^5$ s^{-1})	4.9	1.3
k_{rad} ($\times 10^{-11}$ cm^3 s^{-1})	1.2	
ΔE_t (meV)	74	
P_{esc} (%)	100	

Supplementary Table 5. Defect formation energies for the 3 × 3 × 2 perovskite surface with the neutral and charged V_I, V_{Pb}, Pb_I, and I_{Pb} surface defects.

Charges	V_I	V_{Pb}	Pb_I	I_{Pb}
I-poor/Pb-rich (μ_I = –2.70 eV , μ_{Pb} = –3.85 eV)				
–3			–0.15	2.59
–2		0.03	–0.59	1.57
–1	–2.29	0.05	–0.94	0.50
0	–2.26	0.45	–1.00	2.65
1	–1.71	0.76	–0.86	1.62
2		0.24	0.10	2.36
3			0.26	2.99
I-moderate/Pb-moderate (μ_I = –2.08 eV , μ_{Pb} = –5.08 eV)				
–3			1.71	0.74
–2		–1.20	1.26	–0.28
–1	–1.68	–1.19	0.91	–1.35
0	–1.64	–0.79	0.86	0.80
1	–1.09	–0.47	0.99	–0.23
2		–1.00	1.95	0.51
3			2.11	1.14
I-rich/Pb-poor (μ_I = –1.47 eV , μ_{Pb} = –6.32 eV)				
–3			3.56	–1.11
–2		–2.44	3.11	–2.14
–1	–1.06	–2.42	2.76	–3.20
0	–1.03	–2.02	2.71	–1.05
1	–0.47	–1.71	2.84	–2.08
2		–2.23	3.81	–1.34
3			3.96	–0.72

Supplementary Table 6. Photovoltaic performance of inverted PSCs with Me-4PACz and mixed SAMs.

Device		V_{OC} (V)	J_{SC} (mA cm^{-2})	FF (%)	PCE (%)
Me-4PACz	Best	1.135	25.80	79.53	23.29
	Average	1.103 ± 0.023	25.75 ± 0.19	78.91 ± 0.91	22.24 ± 0.83
BA-Me	Best	1.168	25.90	81.48	24.65
	Average	1.141 ± 0.017	25.96 ± 0.16	80.85 ± 0.70	23.93 ± 0.64
TA-Me	Best	1.179	26.10	82.84	25.49
	Average	1.157 ± 0.018	25.92 ± 0.19	81.98 ± 0.70	24.60 ± 0.51
NA-Me	Best	1.201	26.30	84.50	26.69
	Average	1.185 ± 0.016	26.15 ± 0.18	83.87 ± 0.56	25.95 ± 0.45

Supplementary Table 7. Photovoltaic parameters of the champion inverted PSC with NA-Me under reverse and forward scan.

Scan direction	J_{SC} (mA cm^{-2})	V_{OC} (V)	FF (%)	PCE (%)
Reverse	26.30	1.201	84.50	26.69
Forward	26.35	1.199	84.04	26.55

Supplementary Table 8. Comparison of the photovoltaic performance of inverted PSC in this work with other literature which reported certified PCEs >24%. PCE[a] is extracted from the *J–V* curves and PCE[b] represents the steady-state PCE. Please note that passivation layers in the following devices have been omitted.

Device structure	V_{OC} (V)	J_{SC} (mA cm^{-2})	FF (%)	Certified PCE (%)	Ref.
ITO/MeO-2PACz/$Cs_{0.05}(FA_{0.98}MA_{0.02})_{0.95}Pb(I_{0.98}Br_{0.02})_3$/PCBM/BCP/Ag	1.174	24.84	83.21	24.24[a]	[23]
ITO/NiO_x/MeO-4PADBC/$Cs_{0.05}FA_{0.85}MA_{0.1}PbI_3$/$C_{60}$/BCP/Ag	1.189	25.75	83.54	25.58[a]	[24]
ITO/DC-PA/$Cs_{0.06}MA_{0.14}FA_{0.80}PbI_3$/$C_{60}$/BCP/Ag	1.190	24.45	84.2	24.5[a]	[25]
ITO/Me-4PACz/$(FA_{0.95}MA_{0.05})_{0.95}Cs_{0.05}Pb(I_{0.95}Br_{0.05})_3$/$C_{60}$/BCP/Ag	1.204	24.24	83.06	24.24[a]	[26]
ITO/Me-4PACz/$(FA_{0.95}MA_{0.05})_{0.95}Cs_{0.05}Pb(I_{0.95}Br_{0.05})_3$/$C_{60}$/BCP/Ag	1.203	25.02	82.73	24.90[a]	[22]
ITO/2PACz/$Cs_{0.05}MA_{0.15}FA_{0.80}PbI_3$/$C_{60}$/BCP/Ag	1.160	25.02	83.05	24.09[b]	[27]
FTO/2PACz/$Cs_{0.05}MA_{0.1}FA_{0.85}PbI_3$/$C_{60}$/BCP/Ag	1.150	25.50	84.50	24.80[b]	[21]
FTO/NiO_x/4PACz/$Cs_{0.05}MA_{0.05}FA_{0.90}PbI_3$/$C_{60}$/BCP/Ag	1.170	26.20	84.50	25.90[a]	[28]
ITO/2PACz/$Rb_{0.05}Cs_{0.05}MA_{0.05}FA_{0.85}Pb(I_{0.95}Br_{0.05})_3$/$C_{60}$/BCP/Ag	1.160	26.10	83.82	25.37[a]	[29]
ITO/MPA-CPA/$(FA_{0.95}MA_{0.05})_{0.95}Cs_{0.05}Pb(I_{0.95}Br_{0.05})_3$/$C_{60}$/BCP/Ag	1.21	24.78	84.65	25.39[a]	[30]
ITO/Perovskite (DMAcPA)/PCBM/BCP/Ag	1.189	25.65	83.24	25.39[a]	[31]
FTO/NiO/Me-4PACz/$FAPbI_3$/PCBM/SnO_2/Cu	1.183	26.23	81.20	25.20[b]	[32]
ITO/p-PY/$FA_{0.98}Cs_{0.02}PbI_3$/PCBM/BCP/Ag	1.167	25.80	81.49	24.54[a]	[33]
ITO/NiO/PTAA/Al_2O_3/$Cs_{0.05}FA_{0.95}PbI_3$/PCBM/BCP/Ag	1.173	25.69	81.63	24.60[a]	[34]
ITO/PTAA/$Cs_{0.05}FA_{0.95}PbI_3$/C_{60}/BCP/Ag	1.153	26.50	84.46	25.80[a]	[35]
ITO/NiO/Me-4PACz/$Cs_{0.05}FA_{0.95}PbI_3$/PCBM/BCP/Ag	**1.192**	**26.47**	**84.11**	**26.54[a] (26.54[b])**	**This work**

Supplementary Table 9. Comparison of the PCE of inverted PSCs in this work with other representative literature which involves molecular hybrid for inverted PSCs. PCE[a] is extracted from the *J–V* curves and PCE[b] represents the steady-state PCE. Please note that PVK is the abbreviation form of perovskite. The blackened part refers to the use of molecular hybrid strategies.

Type of SAM	Bandgap of PVK (eV)	PCE (%)	Ref.
MPA-CPA	1.56	25.39[a]	[30]
DMAcPA	1.56	25.39[a]	[31]
MeO-4PADBC	1.53	25.60[a]	[24]
Me-4PACz+ 6dPA	**1.67**	**20.9**	[19]
DC-PA+IAHA	**~1.55**	**23.59**	[20]
2PACz+3-MPA	**~1.53**	**24.8[b]**	[21]
NA-Me	**1.53**	**26.54[b]**	**This work**

Supplementary Table 10. Photovoltaic parameters of minimodule devices (aperture area: 11.1 cm^2) using NA-Me under reverse and forward scan.

Scan direction	J_{SC} (mA cm^{-2})	V_{OC} (V)	FF (%)	PCE (%)
Reverse	4.900	5.811	81.00	23.06
Forward	4.900	5.801	80.55	22.90

Supplementary Table 11. Comparison of the photovoltaic performance of mini-modules (total area larger than10 cm^2) in this work with other representative work which reported PCEs >19%; ac, active area; ap, aperture area; da, designated area (active area + dead area for interconnections). PCE^c is the PCE extracted from the certified *J–V* curves in a third-party certification agency.

Structure	Area (cm^2)	PCE (%)	FF (%)	Ref.
p-i-n	18.1^{ap}	**19.25^c**	**78.00**	[36]
p-i-n	26.9^{ap}	**21.78^c**	**80.32**	[37]
p-i-n	22.0^{ac}	**20.8**	**74.20**	[27]
p-i-n	10^{ac}	**22.0**	**76.9**	[30]
p-i-n	14.65^{ap}	**21.0**	**78.7**	[32]
n-i-p	23.9^{ac}	**22.72^c**	**79.06**	[38]
n-i-p	20^{ac}	**21.66^c**	**77.90**	[39]
Not specified	26.02^{da}	**22.4**	**77.6**	**Record**[40]
p-i-n	11.1^{ap}	**22.74^c**	**80.42**	**This work**

Supplementary Table 12. Comparison of the operational stability under MPPT of inverted PSCs in this work with those of literature which reported certified PCEs >24%. PCE[a] is extracted from the *J–V* curves and PCE[b] represents the steady-state PCE.

Certified PCE (%)	Measured operation lifetime	Ref.
24.24[a]	T_{88} = 1000 hours (75 °C)	[23]
25.58[a]	T_{90} = 1200 hours (65 °C)	[24]
24.5[a]	T_{98} = 1000 hours (65 ± 5 °C)	[25]
24.24[a]	T_{100} = 1000 hours (35-40 °C)	[26]
24.90[a]	T_{98} = 1000 hours (35-40 °C)	[22]
24.09[b]	T_{85} = 1560 hours (85 °C)	[27]
24.80[b]	T_{95} = 1000 hours (65 °C)	[21]
25.90[a]	T_{96} = 2000 hours (65 °C)	[28]
25.37[a]	T_{87} = 2400 hours (55 °C)	[29]
25.39[a]	T_{90} = 2000 hours (45 °C)	[30]
25.39[a]	T_{97} = 1000 hours (RT)	[31]
25.20[b]	T_{85} = 1000 hours (50 °C)	[32]
24.54[a]	T_{97} = 1800 hours (50 ± 5 °C)	[33]
24.60[a]	T_{98} = 1500 hours (55 ± 5 °C)	[34]
25.80[a]	T_{92} = 2500 hours (RT)	[35]
26.54[b]	**T_{96} = 2400 hours (65 °C) (Initial PCE = 26.21% for the operational stability test)**	**This work**

Supplementary References

1. Martínez, L., Andrade, R., Birgin, E. G. & Martínez, J. M. PACKMOL: A package for building initial configurations for molecular dynamics simulations. *J. Comput. Chem.* **30**, 2157-2164 (2009).
2. Thompson, A. P. et al. LAMMPS-a flexible simulation tool for particle-based materials modeling at the atomic, meso, and continuum scales. *Comput. Phys. Commun.* **271**, 108171 (2022).
3. Verlet, L. Computer "experiments" on classical fluids. I. Thermodynamical properties of Lennard-Jones molecules. *Phys. Rev.* **159**, 98 (1967).
4. Nosé, S. A unified formulation of the constant temperature molecular dynamics methods. *J. Chem. Phys.* **81**, 511-519 (1984).
5. Hoover. Canonical dynamics: Equilibrium phase-space distributions. *Phys. Rev. A* **31**, 1695-1697 (1985).
6. Seijas-Bellido, J. A. et al. Transferable classical force field for pure and mixed metal halide perovskites parameterized from first-principles. *J. Chem. Inf. Model.* **62**, 6423-6435 (2022).
7. Mayo, S. L., Olafson, B. D. & Goddard, W. A. DREIDING: a generic force field for molecular simulations. *J. Phys. Chem.* **94**, 8897-8909 (1990).
8. Bayly, C. I., Cieplak, P., Cornell, W. & Kollman, P. A. A well-behaved electrostatic potential based method using charge restraints for deriving atomic charges: the RESP model. *J. Phys. Chem.* **97**, 10269-10280 (1993).
9. Neese, F. Software update: The ORCA program system-Version 5.0. *WIREs. Comput. Mol. Sci.* **12**, e1606 (2022).
10. Rappé, A. K., Casewit, C. J., Colwell, K. S., Goddard III, W. A. & Skiff, W. M. UFF, a full periodic table force field for molecular mechanics and molecular dynamics simulations. *J. Am. Chem. Soc.* **114**, 10024-10035 (1992).
11. Kanhaiya, K. et al. Accurate force fields for atomistic simulations of oxides, hydroxides, and organic hybrid materials up to the micrometer scale. *J. Chem. Theory Comput.* **19**, 8293-8322 (2023).
12. Kresse, G. & Furthmuller, J. Efficient iterative schemes for *ab initio* total-energy calculations using a plane-wave basis set. *Phys. Rev. B* **54**, 11169-11186 (1996).
13. Dudarev, S. L., Botton, G. A., Savrasov, S. Y., Humphreys, C. J. & Sutton, A. P. Electron-energy-loss spectra and the structural stability of nickel oxide: An LSDA+U study. *Phys. Rev. B* **57**, 1505-1509 (1998).
14. Li, F. et al. Regulating surface termination for efficient inverted perovskite solar cells with greater than 23% efficiency. *J. Am. Chem. Soc.* **142**, 20134-20142 (2020).
15. Luo, C. et al. Engineering the buried interface in perovskite solar cells via lattice-matched electron transport layer. *Nat. Photon.* **17**, 856-864 (2023).

16. Ullah, A. et al. Novel phenothiazine-based self-assembled monolayer as a hole Selective contact for highly efficient and stable p-i-n perovskite solar cells. *Adv. Energy Mater.* **12**, 2103175 (2022).
17. Stolterfoht, M. et al. The impact of energy alignment and interfacial recombination on the internal and external open-circuit voltage of perovskite solar cells. *Energy Environ. Sci.* **12**, 2778-2788 (2019).
18. Richter, J. M. et al. Enhancing photoluminescence yields in lead halide perovskites by photon recycling and light out-coupling. *Nat. Commun.* **7**, 13941 (2016).
19. Al-Ashouri, A. et al. Wettability improvement of a carbazole-based hole-selective monolayer for reproducible perovskite solar cells. *ACS Energy Lett.* **8**, 898-900 (2023).
20. Deng, X. et al. Co-assembled monolayers as hole-selective contact for high-performance inverted perovskite solar cells with optimized recombination loss and long-term stability. *Angew. Chem. Int. Ed.* **61**, e202203088 (2022).
21. Park, S. M. et al. Low-loss contacts on textured substrates for inverted perovskite solar cells. *Nature* **624**, 289-294 (2023).
22. Peng, W. et al. Reducing nonradiative recombination in perovskite solar cells with a porous insulator contact. *Science* **379**, 683-690 (2023).
23. Li, G. et al. Highly efficient p-i-n perovskite solar cells that endure temperature variations. *Science* **379**, 399-403 (2023).
24. Li, Z. et al. Stabilized hole-selective layer for high-performance inverted p-i-n perovskite solar cells. *Science* **382**, 284-289 (2023).
25. Li, F. et al. Hydrogen-bond-bridged intermediate for perovskite solar cells with enhanced efficiency and stability. *Nat. Photon.* **17**, 478-484 (2023).
26. Zhu, Z. et al. Correlating the perovskite/polymer multi-mode reactions with deep-level traps in perovskite solar cells. *Joule* **6**, 2849-2868 (2022).
27. Park, S. M. et al. Engineering ligand reactivity enables high-temperature operation of stable perovskite solar cells. *Science* **381**, 209-215 (2023).
28. Liu, C. et al. Bimolecularly passivated interface enables efficient and stable inverted perovskite solar cells. *Science* **382**, 810-815 (2023).
29. Jiang, Q. et al. Surface reaction for efficient and stable inverted perovskite solar cells. *Nature* **611**, 278-283 (2022).
30. Zhang, S. et al. Minimizing buried interfacial defects for efficient inverted perovskite solar cells. *Science* **380**, 404-409 (2023).
31. Tan, Q. et al. Inverted perovskite solar cells using dimethylacridine-based dopants. *Nature* **620**, 545-551 (2023).
32. Yu, S. et al. Homogenized NiO_x nanoparticles for improved hole transport in inverted perovskite solar cells. *Science* **382**, 1399-1404 (2023).

33. Chen, R. et al. Reduction of bulk and surface defects in inverted methylammonium- and bromide-free formamidinium perovskite solar cells. *Nat. Energy* **8**, 839-849 (2023).
34. Li, H. et al. 2D/3D heterojunction engineering at the buried interface towards high-performance inverted methylammonium-free perovskite solar cells. *Nature Energy* **8**, 946-955 (2023).
35. Liang, Z. et al. Homogenizing out-of-plane cation composition in perovskite solar cells. *Nature* **624**, 557-563 (2023).
36. Chen, S. et al. Stabilizing perovskite-substrate interfaces for high-performance perovskite modules. *Science* **373**, 902-907 (2021).
37. Fei, C. et al. Lead-chelating hole-transport layers for efficient and stable perovskite minimodules. *Science* **380**, 823-829 (2023).
38. Ding, Y. et al. Single-crystalline TiO_2 nanoparticles for stable and efficient perovskite modules. *Nat. Nanotechnol.* **17**, 598-605 (2022).
39. Kim, M. et al. Conformal quantum dot-SnO_2 layers as electron transporters for efficient perovskite solar cells. *Science* **375**, 302-306 (2022).
40. Green, M. A. et al. Solar cell efficiency tables (Version 61). *Prog. Photovolt.* **31**, 3-16 (2023).